Computer Methods in Applied Mechanics and Engineering 428 (2024) 117117

Contents lists available at ScienceDirect

Computer Methods in Applied Mechanics and Engineering

journal homepage: www.elsevier.com/locate/cma

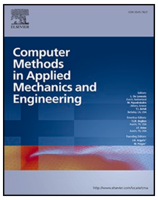

Development of an accurate central finite-difference scheme with a compact stencil for the simulation of unsteady incompressible flows on staggered orthogonal grids

Elyas Larkermani [a,*], Hans Bihs [b], Grégoire Winckelmans [c], Matthieu Duponcheel [c], Tobias Martin [b], Bernhard Müller [a], Laurent Georges [a]

[a] *Department of Energy and Process Engineering (EPT), Norwegian University of Science and Technology (NTNU), Trondheim, Norway*
[b] *Department of Civil and Environmental Engineering, Norwegian University of Science and Technology (NTNU), Trondheim, Norway*
[c] *Institute of Mechanics, Materials, and Civil Engineering (iMMC), Université Catholique de Louvain (UCLouvain), Louvain-la-Neuve, Belgium*

ARTICLE INFO

Keywords:
Finite difference method
Large Eddy Simulation
Incompressible flow
Staggered grid

ABSTRACT

In scale-resolving simulations such as Large Eddy Simulations (LES), the spatial discretization scheme of the convective term plays a crucial role in avoiding interference between the numerical errors and the subgrid-scale model. Accurate schemes lead to lower truncation errors and better predictions of turbulent flows without the need for an excessively refined grid. To this end, a new second-order finite-difference scheme (HCDS6) has been developed for incompressible flows and orthogonal staggered grids. Compared to the standard second-order scheme, the new scheme has significantly lower dispersion errors. Compared to existing high-order schemes, the numerical stencil of HCDS6 is more compact, which makes it easier to implement, especially considering boundary conditions around complex geometries using Immersed Boundary Methods (IBM). The HCDS6 scheme conserves the discrete momentum with limited production or dissipation of discrete kinetic energy, which guarantees its numerical stability. Its performance is evaluated using an open-source CFD package called REEF3D. Three benchmarks demonstrate the key properties and performance of the scheme: the convection of an isentropic vortex, the Taylor-Green vortex flow, and turbulent channel flow. Its relatively low dispersion errors, combined with ease of implementation, make the HCDS6 scheme a promising candidate for efficient scale-resolving simulations of turbulent flows.

1. Introduction

This research aims to construct an accurate finite-difference scheme for incompressible unsteady turbulent flow simulations such as Large Eddy Simulations (LES) or Direct Numerical Simulations (DNS). More specifically, the paper focuses on the convective term of the momentum equation. It considers orthogonal non-uniform grids where complex geometries can be considered using Immersed Boundary Methods (IBM) [1]. In this context, as many different numerical methods can be applied, the introduction will first define the specific framework of our study.

Previous studies [2-7] have demonstrated the significant influence of numerical errors on the prediction accuracy of LES.

---

* Corresponding author
E-mail address: elyas.larkermani@ntnu.no (E. Larkermani).

https://doi.org/10.1016/j.cma.2024.117117
Received 6 March 2024; Received in revised form 1 June 2024; Accepted 1 June 2024

Significant kinetic energy at high wavenumbers in LES requires a numerical scheme that performs well in this range. Although spectral methods are known for their uniform accuracy at all wavenumbers, they do have inherent limitations concerning geometry and boundary conditions, which makes them less applicable in practical cases involving irregular or complex geometries [8]. Furthermore, aliasing errors are important when using spectral methods. Unless explicitly removed using filtering techniques, these errors can lead to a degradation of the solution and negatively impact the accuracy of the simulation [9]. Finite difference, finite volume and finite element methods have lower aliasing errors due to the damping at high wavenumbers [9]. They are often preferred in practical LES applications due to their computational efficiency and flexibility for boundary conditions [10]. For these numerical methods, the conservation of the discrete kinetic energy is an important property for the spatial discretization of the convective term of the momentum equation. Turbulence is characterized by kinetic energy transfer between the different turbulent flow scales. Therefore, the numerical scheme should not interfere in this process through artificial numerical dissipation. In explicit LES, the kinetic energy dissipation at smaller flow scales should be left to the subgrid-scale (SGS) model. Central schemes are known to be non-dissipative, but generally, they do not conserve the discrete kinetic energy. In practice, this may affect the numerical stability of under-resolved simulations, such as LES. Only a subset of central schemes has been tailored to enforce the discrete kinetic energy conservation (assuming negligible time integration errors), which guarantees numerical stability [11,12].

Collocated grids placing all the flow variables (i.e., the velocity and pressure fields) at the same points leads to the checkerboard problem (i.e., spurious pressure oscillations). This effect can be avoided by using stabilization or special interpolation techniques [13]. Although popular and widely used in LES, these techniques introduce some numerical dissipation [14]. Alternatively, the staggered grid arrangement does not suffer from the checkerboard problem by placing flow variables at different locations. This arrangement is challenging to apply for complex grids, such as unstructured grids. However, the complexity is acceptable for orthogonal non-uniform grids, as discussed in this paper. Finally, it is also worth mentioning that Laizet and Lamballais [10] managed to introduce a high-order compact scheme for incompressible flow on orthogonal grids by using a semi-staggered arrangement (meaning that all the velocity components are located at the same point, except for pressure).

The remainder of the paper discusses central finite differences on staggered orthogonal grids, with a special focus on the conservation of the discrete kinetic energy by the convective term. Existing schemes in this category will be discussed to introduce the originality of the new scheme proposed in the paper.

- One remarkable example is the second-order central finite-difference scheme developed by Harlow and Welch for staggered meshes [15]. It has proved to be well-suited for DNS and LES of turbulent flow [16-19]. This scheme conserves not only the discrete mass and momentum but also the discrete kinetic energy on a uniform grid. Vasilyev [11] analyzed the conservation properties of finite differences on non-uniform staggered grids. In finite differences, the convective term can be discretized into three different forms: the divergence, advective and skew-symmetric forms. Vasilyev demonstrated that his second-order discretization cannot simultaneously conserve the discrete momentum and kinetic energy on a non-uniform mesh (called “commutation error” in [11]). In the divergence form, the scheme conserves discrete momentum on a non-uniform grid, while the conservation of discrete kinetic energy is limited to a uniform grid. In contrast, in the skew-symmetric form, the scheme exhibits the opposite behavior. Verstappen et al. [12] introduced a second-order finite volume scheme on non-uniform staggered grids. As it is a finite volume method, it inherently conserves the discrete momentum, but it also manages to conserve the discrete kinetic energy.
- In these schemes for non-uniform grids, the coefficients of the numerical stencil are not adapted locally as a function of the local grid-stretching to conserve the skew-symmetry property of the discretization operator. By preserving the skew-symmetry property of the operator, the discrete kinetic energy is conserved. As the coefficients are not adapted to the local grid-stretching, it leads to a local truncation error that is first order. Nevertheless, studies by Rivas (referenced by Eq. (1) in her article [20]) and Manteufel and White [21] have demonstrated that these schemes can achieve second-order accuracy on non-uniform grids.
- Although widely used for simplicity and efficiency, the second-order central scheme has large dispersion errors. Higher-order numerical schemes overcome the impact of truncation errors, thereby providing more accurate approximations and improving the fidelity of the resolved scales [22]. Morinishi et al. [23] introduced high-order finite differences (i.e., fourth-order and higher) on staggered orthogonal grids that conserve the discrete momentum and kinetic energy on uniform meshes. Vasilyev extended these schemes to non-uniform grids [11]. Similar conclusions apply to the fourth-order schemes as observed in the second-order central schemes. Among the three forms of the fourth-order finite difference schemes introduced by Vasilyev, none can simultaneously conserve both discrete momentum and kinetic energy. However, the fourth-order finite volume scheme by Verstappen et al. [12] proves to achieve this conservation. The main challenge with these two schemes is that the numerical stencil is not compact due to the use of high-order interpolations. From second- to fourth-order accuracy, these numerical stencils are not only increased from three to seven points along lines for the three spatial directions but also expanded from two to four points in the perpendicular directions to each line. These schemes are thus more complex to implement, and they make the treatment of boundary conditions more complicated, particularly when dealing with complex geometries in practical engineering applications using IBM.

The paper, therefore, introduces a new second-order numerical scheme on staggered grids with lower dispersion errors than the conventional second-order schemes of Vasilyev [11] and Verstappen et al. [12]. The new scheme involves seven points in each spatial direction, but unlike the existing fourth-order schemes on staggered grids, the numerical stencil remains compact. This simplifies the implementation and the treatment of boundary conditions. Although the scheme is formally second-order accurate, it is six-order accurate for linear advection problems, providing relatively low dispersion errors. Finally, the strict conservation of the discrete kinetic energy has to be sacrificed to enable this improvement. Still, the numerical tests introduced in the paper prove that this has a limited impact on results for LES. The key properties of the new scheme are evaluated using three benchmarks: the convection of an isentropic vortex, the three-dimensional Taylor-Green vortex flow, and the turbulent channel flow simulation.

The paper is organized as follows. In Section 2, the discrete equations for the incompressible Navier-Stokes equations and the new scheme are introduced. Section 3 analyzes the performance of the new scheme against the three flow benchmarks. Section 4 concludes the paper by summarizing the findings and outlining future research directions.

2. Numerical method

2.1. Governing equations

The incompressible Navier-Stokes equations are presented in Eq. (1) and translate the mass conservation and Newton's second law:

$$\begin{aligned} \frac{\partial u_m}{\partial x_m} &= 0 \\ \frac{\partial u_m}{\partial t} + \frac{\partial}{\partial x_n}(u_m u_n) &= -\frac{1}{\rho}\frac{\partial p}{\partial x_m} + \upsilon \frac{\partial^2 u_m}{\partial {x_n}^2} \end{aligned} \tag{1}$$

where x_m denotes the m^{th} spatial coordinate direction in the physical space, u_m represents the velocity field in the x_m direction. Here, the Einstein summation convention is used, where repeated indices imply summation. Parameter t is the time, p is the pressure, υ is the kinematic viscosity and ρ is the density. They are assumed to be constant – i.e., independent of the temperature.

2.2. Spatial discretization

A schematic representation of a two-dimensional fully staggered grid arrangement where the velocity components are located at the cell surfaces while the pressure and other scalar quantities are stored in the cell center [13] is illustrated in Fig. 1. Here, i and j are mesh indices in the x_1 and x_2 directions, respectively.

In our work, the discretization operation is performed in computational space to preserve symmetries of the underlying operator. The derivatives in physical space are calculated using the local Jacobian, which can be determined numerically using the same stencil and corresponding weights as the finite differencing operator in the computational space with a uniform grid [11]. In a one-dimensional case, this gives:

$$\frac{\delta\phi}{\delta x} = \frac{1}{J}\frac{\delta\phi}{\delta\zeta} = \frac{1}{J}\frac{\phi_{i+1} - \phi_{i-1}}{2\Delta} \tag{2}$$

In the above definition, ζ denotes the spatial coordinate in the computational domain, and ϕ represents a discrete variable in three spatial coordinate directions. J is the Jacobian of the transformation $x \rightarrow \zeta$ that can be defined numerically as:

$$J = \frac{\delta x}{\delta\zeta} = \frac{x_{i+1} - x_{i-1}}{2\Delta} \tag{3}$$

where Δ is the uniform grid spacing in the computational domain.

Using the notation of Morinishi et al. [23], the finite difference operator $(\delta_n/\delta_n\zeta_1)$ with respect to ζ_1 and the interpolation operator $(\overline{\phi}^{n\zeta_1})$ in the ζ_1 direction in computational space with a stencil n acting on the field ϕ are respectively defined as:

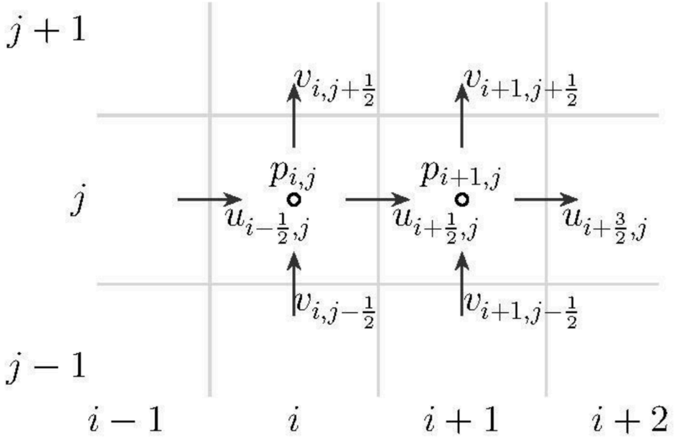

Fig. 1. Staggered arrangement of variables in two dimensions.

$$
\begin{aligned}
\frac{\delta_n \phi}{\delta_n \zeta_1}\Big|_{\zeta_1,\zeta_2,\zeta_3} &= \frac{\phi(\zeta_1 + n\Delta_1/2, \zeta_2, \zeta_3) - \phi(\zeta_1 - n\Delta_1/2, \zeta_2, \zeta_3)}{n\Delta_1} \\
\overline{\phi}^{n\zeta_1}\Big|_{\zeta_1,\zeta_2,\zeta_3} &= \frac{\phi(\zeta_1 + n\Delta_1/2, \zeta_2, \zeta_3) + \phi(\zeta_1 - n\Delta_1/2, \zeta_2, \zeta_3)}{2}
\end{aligned}
\tag{4}
$$

These two operators can be extended to the other spatial directions. Following these operators, the standard second-order scheme of Vasilyev for the non-linear convective term in Eq. (1) on a non-uniform staggered grid is defined as:

$$
\begin{aligned}
(\text{Div.})_m &= \frac{\delta(u_n u_m)}{\delta \zeta_n} = \frac{\delta_1}{\delta_1 \zeta_n}\left\{\overline{u}_n^{1\zeta_m}\overline{u}_m^{1\zeta_n}\right\} \\
(\text{Adv.})_m &= u_n \frac{\delta(u_m)}{\delta \zeta_n} = \frac{1}{J_n}\left[\overline{\overline{u}_n^{1\zeta_m}\frac{\delta_1 u_m}{\delta_1 \zeta_n}}^{1\zeta_n}\right] \\
(\text{Skew.})_m &= \frac{1}{2}(\text{Div.})_m + \frac{1}{2}(\text{Adv.})_m
\end{aligned}
\tag{5}
$$

This scheme in divergence form, here termed CDS2, conserves the discrete momentum on a non-uniform mesh, while the discrete kinetic energy is conserved only on a uniform mesh. The new scheme (HCDS6) also employs the divergence form for the convective term, using an original hybrid formulation for its discretization. It uses a symmetric, seven-point stencil where the convection velocity is interpolated with a second-order accurate interpolation operator, whereas the convective fluxes are discretized using a high-order central interpolation scheme:

$$
\frac{\delta(u_n u_m)}{\delta x_n} = \frac{\delta_1}{\delta_1 x_n}\left\{\overline{u}_n^{\,1x_m}\left(\alpha_1 \overline{u}_m^{\,1x_n} + \alpha_3 \overline{u}_m^{\,3x_n} + \alpha_5 \overline{u}_m^{\,5x_n}\right)\right\}
\tag{6}
$$

with α_1, α_3, and α_5 being the constant scheme coefficients, not adapted according to the local grid-stretching. The coefficients $\alpha_1 = 37/30$, $\alpha_3 = -8/30$, and $\alpha_5 = 1/30$ are chosen such that Eq. (6) corresponds to the standard sixth-order central difference approximation for a constant convection velocity (see Section 2.3). For $\alpha_1 = 1$, $\alpha_3 = 0$, and $\alpha_5 = 0$, the method is degraded to the standard second-order central differential scheme of Vasilyev (CDS2). The HCDS6 is thus tailored to reduce dispersion errors compared to the CDS2. However, the conservation of the discrete kinetic energy had to be sacrificed for this purpose. The HCDS6 conserves the discrete

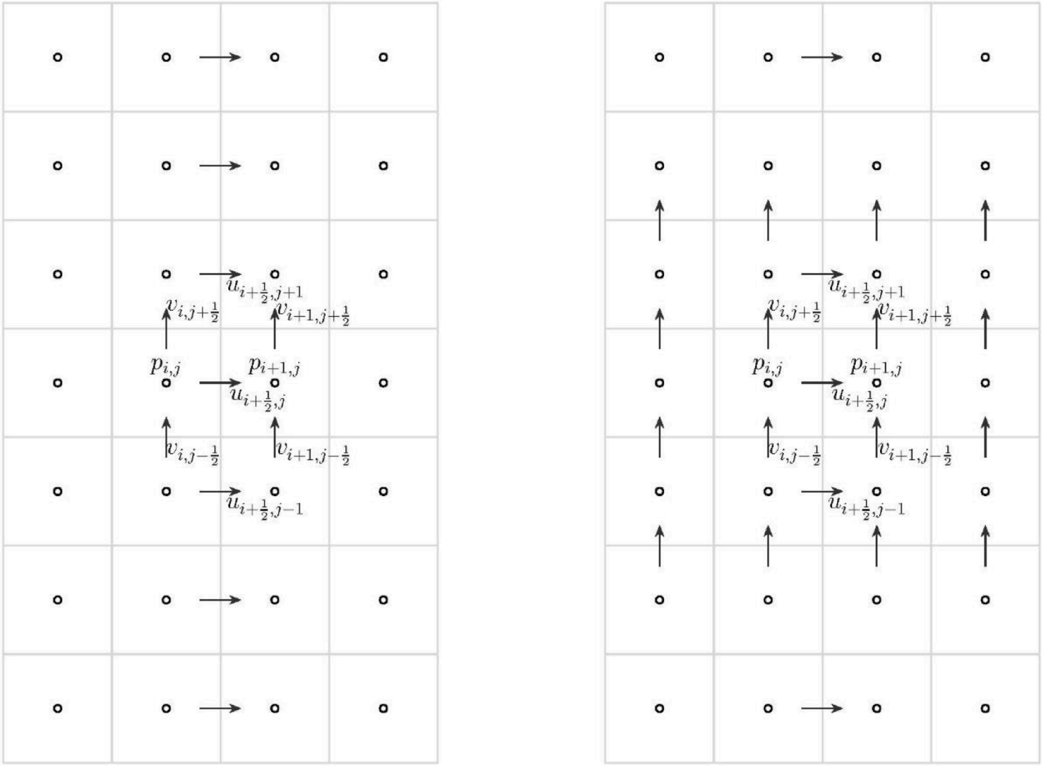

(*a*) (*b*)

Fig. 2. Comparison of the numerical stencil for HCDS6 (***a***) and CDS4 (***b***) for $\boldsymbol{m} = 1$ and $\boldsymbol{n} = 2$.

momentum on non-uniform grids; however, it does not conserve the discrete kinetic energy, even in the case of uniform grids. However, results will show that this effect remains limited as the stencil weights are not adapted according to the local grid-stretching.

It can be observed that the new HCDS6 and CDS2 schemes are more compact than the fourth-order finite-difference schemes of Vasilyev [11] – for example, in divergence form (CDS4):

$$\frac{\delta(u_n u_m)}{\delta x_n} = \frac{9}{8}\,\frac{\delta_1}{\delta_1 x_n}\left\{\left(\frac{9}{8}\overline{u}_n^{1x_m} - \frac{1}{8}\overline{u}_n^{3x_m}\right)\overline{u}_m^{1x_n}\right\} - \frac{1}{8}\,\frac{\delta_3}{\delta_3 x_n}\left\{\left(\frac{9}{8}\overline{u}_n^{1x_m} - \frac{1}{8}\overline{u_n}^{3x_m}\right)\overline{u_m}^{3x_n}\right\} \tag{7}$$

The term compact stencil should not be confused with compact finite difference schemes [24]. A compact stencil here means that the spatial extension of the points involved in the numerical stencil remains localized in a limited volume. Like the HCDS6, the CDS4 has a seven-point stencil in each spatial direction. However, in contrast to the HCDS6, the CDS4 computes the convection velocity using a fourth-order interpolation. As a result, CDS4 has a stencil that involves four points in the directions perpendicular to each spatial direction, making the stencil not compact, see Fig. 2.

Using the definition of the finite difference and the interpolation operators in Eq. (4) at the mesh indexes i, j, and k, the new central scheme (HCDS6) for the convective terms on staggered grids can be rewritten for the momentum equation in the direction x_1. To simplify the notation, u_1 and u_2 are simplified to u and v, and x_1 and x_2 to x and y, respectively:

$$\begin{aligned}
\frac{\delta(uu)}{\delta x}\Big|_{i+1/2,j,k} &= \frac{\frac{u_{i+1/2,j,k}+u_{i+3/2,j,k}}{2}\left(\alpha_1\frac{u_{i+1/2,j,k}+u_{i+3/2,j,k}}{2}+\alpha_3\frac{u_{i-1/2,j,k}+u_{i+5/2,j,k}}{2}+\alpha_5\frac{u_{i-3/2,j,k}+u_{i+7/2,j,k}}{2}\right)}{x_{i+1}-x_i} \\
&- \frac{\frac{u_{i-1/2,j,k}+u_{i+1/2,j,k}}{2}\left(\alpha_1\frac{u_{i-1/2,j,k}+u_{i+1/2,j,k}}{2}+\alpha_3\frac{u_{i-3/2,j,k}+u_{i+3/2,j,k}}{2}+\alpha_5\frac{u_{i-5/2,j,k}+u_{i+5/2,j,k}}{2}\right)}{x_{i+1}-x_i} \\
\frac{\delta(vu)}{\delta y}\Big|_{i+1/2,j,k} &= \frac{\frac{v_{i,j+1/2,k}+v_{i+1,j+1/2,k}}{2}\left(\alpha_1\frac{u_{i+1/2,j,k}+u_{i+1/2,j+1,k}}{2}+\alpha_3\frac{u_{i+1/2,j-1,k}+u_{i+1/2,j+2,k}}{2}+\alpha_5\frac{u_{i+1/2,j-2,k}+u_{i+1/2,j+3,k}}{2}\right)}{y_{j+1/2}-y_{j-1/2}} \\
&- \frac{\frac{v_{i,j-1/2,k}+v_{i+1,j-1/2,k}}{2}\left(\alpha_1\frac{u_{i+1/2,j-1,k}+u_{i+1/2,j,k}}{2}+\alpha_3\frac{u_{i+1/2,j-2,k}+u_{i+1/2,j+1,k}}{2}+\alpha_5\frac{u_{i+1/2,j-3,k}+u_{i+1/2,j+2,k}}{2}\right)}{y_{j+1/2}-y_{j-1/2}}
\end{aligned} \tag{8}$$

Compared to the CDS2, the HCDS6 scheme does not significantly increase the computational time to evaluate the momentum equation in the inner part of the computational domain. However, the situation is different near the boundaries, as the numerical stencil of HCDS6 has seven points in each spatial direction. Firstly, this means that three layers of ghost points need to be created for Dirichlet and Neumann boundary conditions. Secondly, in parallel computation, three layers of points must be exchanged between partitions considering a multi-block domain decomposition. This increases the amount of data to be exchanged between processors, in contrast to the CDS2, which only requires the communication of one layer of points. The spatial discretization of the continuity equation is the same for the CDS2 and HCDS6 schemes. The computational time related to solving the continuity equation is thus identical for both schemes, for instance, to solve the Poisson equation in the context of a projection method (see Section 2.4).

2.3. Linear advection problem

Consider the 1D linear advection equation of the form:

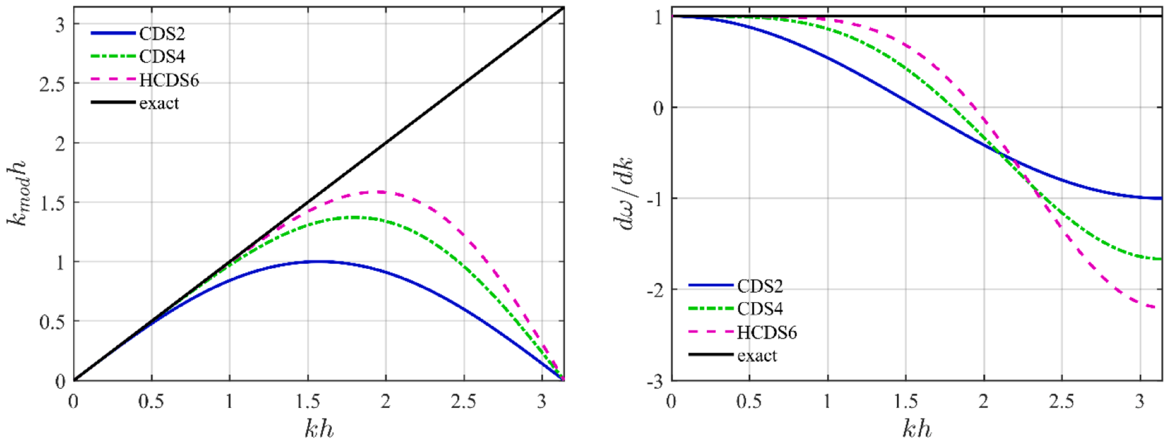

(a) (b)

Fig. 3. Non-dimensional modified wavenumber (**a**) and group velocity (**b**) for $\boldsymbol{a} = 1$ with CDS2, CDS4, and HCDS6.

$$\frac{\partial u}{\partial t}+a\frac{\partial u}{\partial x}=0 \tag{9}$$

where a is the constant advection velocity on the spatial domain $x\in[0,2\pi]$ with periodic boundary conditions. Using the new central difference scheme (HCDS6) defined in Eq. (6) to discretize the convective term on a uniform mesh ($\Delta x=h$), the semi-discretized one-dimensional linear advection equation is obtained:

$$\frac{\partial u_i}{\partial t}+\left[a\frac{\delta_1}{\delta_1 x_i}\left(\frac{37}{30}\overline{u}_i^{1x_i}-\frac{8}{30}\overline{u}_i^{3x_i}+\frac{1}{30}\overline{u}_i^{5x_i}\right)\right]_{x_i,y_j,z_k}=0 \tag{10}$$

$$\frac{\partial u_i}{\partial t}+\frac{a}{2h}\left(\frac{1}{30}u_{i+3}-\frac{3}{10}u_{i+2}+\frac{3}{2}u_{i+1}-\frac{3}{2}u_{i-1}+\frac{3}{10}u_{i-2}-\frac{1}{30}u_{i-3}\right)=0 \tag{11}$$

This spatial discretization is six-order accurate, which explains why the new scheme has been given the acronym HCDS6. The modified wavenumber analysis can be performed. The details of the mathematical developments are given in the Appendix. Fig. 3(a) shows that the non-dimensional modified wavenumber ($k_{mod}h$) of the CDS2 and HCDS6 schemes almost follow the exact wavenumber up to about $\xi=kh=0.4$ and 1.2, respectively. The non-dimensional modified wavenumber for CDS2 decreases from the maximum at $\xi=\pi/2$ to zero at $\xi=\pi$, while the $k_{mod}h$ for HCDS6 stays near the exact solution even at $\xi=\pi/2$, where $k_{mod}h=1.47$.

The group velocity ($d\omega/dk$) is the velocity at which groups of waves and also energy are transported. Fig. 3(b) indicates that HCDS6 computes the group velocity more correctly than CDS2. For $\xi\geq\pi/2$, groups of waves and energy are transported in the wrong direction with CDS2, whilst they are transported in the right direction with HCDS6. For $\xi=\pi$, $d\omega/dk=-a$ for CDS2, and $d\omega/dk=-2.2a$ for HCDS6. Remember that the exact group velocity is a.

As HCDS6 better represents the phase velocity and group velocity at higher wavenumbers than CDS2, fewer points per wavelength are required for HCDS6 than for CDS2. This can significantly reduce the number of grid points in three dimensions to reach the same accuracy. It is worth noting that, for a linear advection problem, the performance of HCDS6 is superior to the fourth-order accurate scheme of Vasilyev [11] (CDS4). The analysis of the phase speed anisotropy is given in the Appendix.

2.4. REEF3D solver package

REEF3D is an open-source CFD software package that focuses on CFD in hydrodynamics, environmental, and marine engineering. In REEF3D, physical models, numerical methods and solvers are implemented as a collection of C++ classes and objects. The object-oriented design of REEF3D makes the code extendable and easy to customize. Users can modify existing solvers or create new ones by subclassing and extending the existing classes. REEF3D uses a ghost-cell immersed-boundary method to deal with complex geometry on an orthogonal grid [25]. The ghost-cell method belongs to the general category of IBM, which can potentially treat arbitrary immersed bodies on orthogonal meshes [26]. In REEF3D, the incompressible Navier-Stokes equations are solved in parallel using domain decomposition. Partitions communicate with their neighbors using ghost cells and the Message Passing Interface (MPI) [27]. The current simulations were performed on the FRAM cluster provided by UNINETT Sigma2, which is the National Infrastructure for High-Performance Computing and Data Storage in Norway. It is a distributed memory system that consists of 1,004 dual-socket and two quad-socket nodes, interconnected with a high-bandwidth, low-latency Infiniband network. The interconnect network is organized in an island topology, with 9,216 cores in each island. Each standard compute node has two 16-core Intel Broadwell chips (2.1 GHz) and 64 GiB memory. In addition, eight larger memory nodes with 512 GiB RAM are available, catering to computational tasks that demand substantial memory resources for more complex simulations and data-intensive processing. The total number of compute cores is 32,256.

In REEF3D, the pressure velocity coupling is ensured by using the projection method proposed by Chorin [28]. Here, the computation of velocity and pressure is decoupled and performed in three steps. During the first step, the method proceeds by neglecting the incompressibility constraint to compute an intermediate velocity field u^* using Eq. (12):

$$\frac{u_m^*-u_m^k}{\Delta t}+\frac{\delta}{\delta x_n}\left(u_n^k u_m^k\right)=-\frac{1}{\rho}\frac{\delta p^k}{\delta x_m}+\frac{\delta}{\delta x_n}\left[\upsilon\left(\frac{\delta u_m^k}{\delta x_n}+\frac{\delta u_n^k}{\delta x_m}\right)\right] \tag{12}$$

where u_m^k is the velocity at k^{th} time step. Note that the resulting intermediate velocity u_m^* does not satisfy the continuity equation (Eq. (1)). To enforce continuity, the intermediate velocity is projected onto the space of incompressible divergence-free vector fields to obtain u_m^{k+1}:

$$\frac{u_m^{k+1}-u_m^*}{\Delta t}=-\frac{1}{\rho}\frac{\delta_1\left(p^{k+1}-p^k\right)}{\delta_1 x_m} \tag{13}$$

This is done by solving a Poisson equation for the pressure field, using the divergence of the intermediate velocity field and enforcing $\delta_1 u_m^{k+1}/\delta_1 x_m=0$. The fully parallelized Bi-Conjugate Gradients Stabilized (BiCGStab) algorithm [29] solves the resulting Poisson pressure equation by using geometric multigrid preconditioning provided by the high-performance solver library, HYPRE [30].

$$\frac{\delta_1}{\delta_1 x_m}\left(\frac{1}{\rho}\frac{\delta_1\left(p^{k+1}-p^k\right)}{\delta_1 x_m}\right) = -\frac{1}{\Delta t}\frac{\delta_1 u_m^*}{\delta_1 x_m} \tag{14}$$

The result is a pressure field that enforces the incompressibility constraint on the velocity field. Finally, the new velocity field u_m^{k+1} at time step $k+1$ is obtained by subtracting the gradient of the pressure field scaled by $\Delta t/\rho$ from intermediate velocity (Eq. (13)). This results in a velocity field that satisfies both the momentum and continuity equations. It is noteworthy that Eq. (13) is strictly the same for CDS2 and HCDS6.

By default, the governing equations are advanced in time using a fully explicit third-order Total Variation Diminishing (TVD) Runge-Kutta scheme [31]. At each Runge-Kutta stage, Chorin's projection method is applied so that all the substep velocity fields are divergence-free, and the Poisson equation is solved three times per time step [32].

For the viscous terms, the second-order central difference scheme is adopted (i.e., the same for CDS2 and HCDS6):

$$\frac{\delta}{\delta x_n}\left[\frac{\delta u_m}{\delta x_n}\right]\Big|_{i,j,k} = \frac{\delta_1}{\delta_1 x_n}\left\{\frac{\delta_1 u_m}{\delta_1 x_n}\right\}\Big|_{i,j,k} \tag{15}$$

3. Validation tests

This section describes three benchmark tests that were carried out in the REEF3D flow solver [27] to demonstrate the properties and performance of the present numerical method, including the convection of an isentropic vortex, the three-dimensional Taylor--Green vortex flow, and turbulent channel flow simulations.

3.1. Convection of an isentropic vortex

In order to test the performance of the HCDS6 scheme concerning its dissipation and dispersion properties, the convection of a two-dimensional isentropic vortex is considered using incompressible Euler equations. The vortex is convected by a uniform flow in the positive x direction. The initial solution is represented by the velocity components in the x and y directions:

$$\begin{pmatrix} u \\ v \end{pmatrix} = \begin{pmatrix} u_\infty \\ 0 \end{pmatrix} + u_A e^{\left(1-(r/b)^2\right)/2}\begin{pmatrix} (y-y_0)/b \\ -(x-x_0)/b \end{pmatrix} \tag{16}$$

with $r^2 = (x-x_0)^2 + (y-y_0)^2$ being the distance from the vortex center (x_0, y_0). The circumferential velocity induced by the vortex reaches its maximum value (u_A) at $r = b$. The vortex is translated with a mean-flow velocity in the x direction within a two-dimensional periodic domain. To minimize the impact of the boundary conditions and geometry on the results, a large computational domain $[-25L, 25L]^2$ is considered. Here $L = \sqrt{\ln 2}b$ is a representative length scale of the vortex where $e^{-(r/b)^2} = 1/2$ at $r = L$.

A strong vortex with $u_A/u_\infty = 0.8$ is convected from the initial location at $(x_0, y_0) = (-18.75L, 0)$ to the final position $(x, y) = (18.75L, 0)$ for a time period of $u_\infty t/L = 37.5$ on a uniform Cartesian grid. The Courant number is selected to be extremely small $(CFL = 1.152e-3)$ on the finest grid so that the effect of time discretization error is negligible.

3.1.1. Verification and consistency

The Root-Mean-Square (RMS) error between the numerical and analytical solutions as a function of the grid resolution for the CDS2

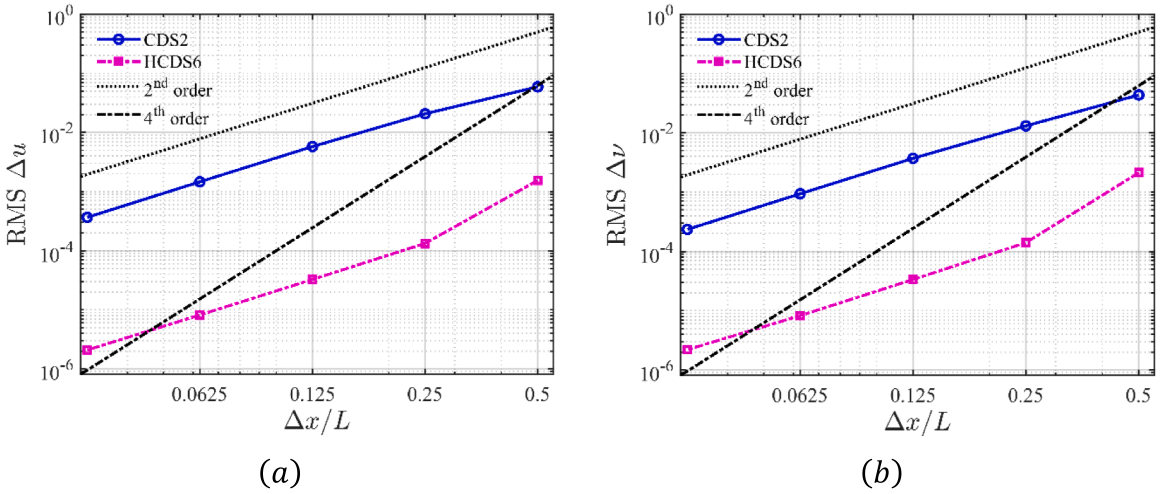

Fig. 4. Convection of strong isentropic vortex on a uniform grid: grid dependence of the root-mean-square value of difference with the analytical solution at the time $u_\infty t/L = 37.5$. (***a***): velocity component u, (***b***): velocity component v.

and HCDS6 schemes is shown in Fig. 4.

This shows that the HCDS6 scheme is indeed second-order accurate. For cell sizes smaller than $L/4$, the discretization error of second-order starts to dominate the global error. However, the error is reduced by approximately two orders of magnitude for the HCDS6, compared to the standard CDS2.

3.1.2. Shape and position of the vortex

The local resolution of the vortex on two different grid sizes ($\Delta x = L/2,\ L/4$) is shown in Fig. 5. Here, the y velocity component along the midline at $y = 0$ is compared with the analytical solution. For CDS2, the vortex has clearly lost its shape on a coarse grid ($\Delta x = L/2$), whilst it is better preserved by the lower dispersion error of the HCDS6. A close agreement with the analytical curve is achieved. As the mesh is further refined, the vortex shape is improved significantly by the CDS2 scheme, whilst the improvement for HCDS6 is minor as the solution was already accurate on the coarser mesh. The vortex center drifted upward using the CDS2 scheme due to the dispersion error, as indicated by a smaller difference between the numerical and analytical solution for the positive peak than for the negative one. In other words, the vortex consists of a collection of waves with different wavelengths that are propagated at different velocities. Using the CDS2 scheme, the waves with low wavenumbers are propagated at the correct speed, whilst those with higher wavenumbers travel at the wrong speed. Consequently, those that are not propagated correctly are lagging and oscillating as a result of

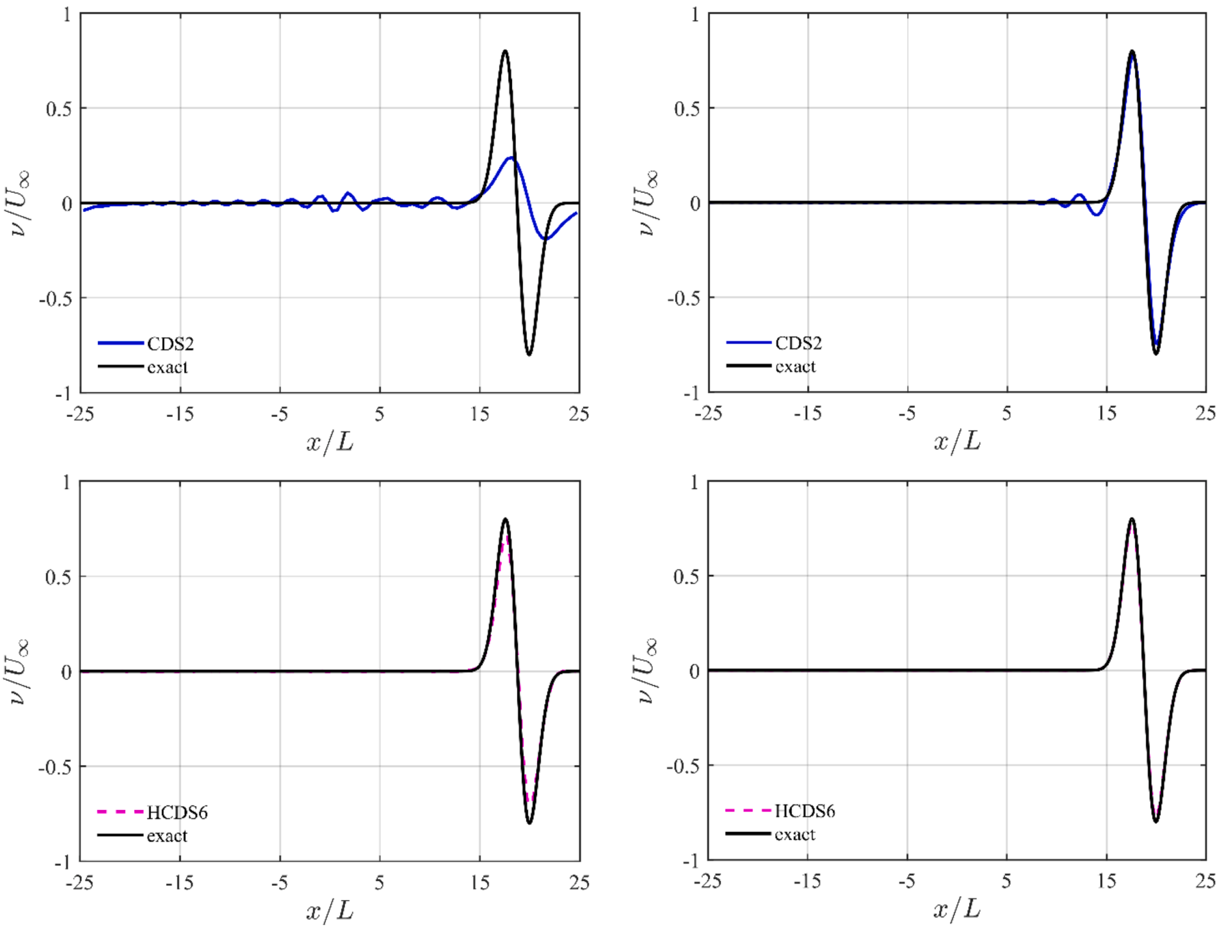

Fig. 5. y velocity component along the midline at $\boldsymbol{y} = 0$. Left: coarse grid ($\boldsymbol{\Delta x} = \boldsymbol{L}/2$), right: fine grid ($\boldsymbol{\Delta x} = \boldsymbol{L}/4$).

Table 1
Comparison of the execution time of the CDS2 and HCDS6 for the convection of an isentropic vortex.

Δx	n_t	$t_{\text{CDS2}}[s]$	r_{CDS2}	$t_{\text{HCDS6}}[s]$	r_{HCDS6}	$t_{\text{HCDS6}}/t_{\text{CDS2}}$
$L/2$	1.88e6	2.98e4	-	2.96e4	-	0.99
$L/4$	1.88e6	7.19e4	2.41	7.35e4	2.48	1.02
$L/8$	1.88e6	2.01e5	2.80	2.08e5	2.83	1.03
$L/16$	1.88e6	2.73e5	1.36	2.78e5	1.34	1.02
$L/32$	1.88e6	8.07e5	2.95	8.72e5	3.13	1.08

the dispersion error. In addition, the amplitude of low wavenumbers is carried correctly. In contrast, the amplitude carried by the higher wavenumbers appears as oscillation and reduces the vortex peak amplitude. The HCDS6 outperforms the CDS2 in maintaining the shape and position of the vortex.

The computational time of both numerical schemes $(t_{\mathrm{CDS2}}, t_{\mathrm{HCDS6}})$ is shown in Table 1. The required wall-clock time to convect the vortex from the initial position to the final position with a time step of $\Delta t = 2e-5s$ is almost identical $(t_{\mathrm{HCDS6}}/t_{\mathrm{CDS2}} \approx 1)$ for both CDS2 and HCDS6. It should be noted that the additional computational time to evaluate this test case using the HCDS6 scheme compared to the CDS2 scheme is small. A main reason is related to the resolution of the Poisson equation for the pressure. It takes most of the CPU time per time step, while the spatial discretization of this equation is identical for both the CDS2 and HCDS6 schemes.

The ratio of the wall-clock time of each numerical scheme to the time required by the same scheme on the next coarser grid is defined by r when the grid is refined consecutively. This ratio is almost similar for both CDS2 and HCDS6 and about 6 percent higher for HCDS6 on the finest grid. This ratio shows a significant reduction when the grid is refined from $\Delta x = L/8$ to $\Delta x = L/16$ due to an increase in the number of processors.

3.2. 3D Taylor-Green vortex flow

The Taylor-Green vortex flow is a well-defined, transient, three-dimensional flow that is generated by the interaction of two counter-rotating vortices in a periodic cubic domain. This classic benchmark problem is typically used to validate numerical methods for scale-resolving simulations [33]. Interactions between different scales of motion in the fluid are driven by the non-linear advection term in the Navier-Stokes equations. These interactions create smaller-scale vortices through vortex stretching, filamentation, and reconnection. These features are responsible for transferring energy from large-scale motion to smaller scales through the energy cascade.

The counter-rotating vortices are initialized in a checkerboard arrangement from an analytical periodic vortex field where a sinusoidal velocity field with a uniform vorticity distribution in the x-y plane is specified:

$$\begin{aligned}\frac{u}{U} &= \sin\left(\frac{x}{L}\right)\cos\left(\frac{y}{L}\right)\cos\left(\frac{z}{L}\right)\\ \frac{v}{U} &= -\cos\left(\frac{x}{L}\right)\sin\left(\frac{y}{L}\right)\cos\left(\frac{z}{L}\right)\\ \frac{w}{U} &= 0\end{aligned} \tag{17}$$

where L and U are the characteristic length and velocity scales of the problem, respectively. The Reynolds number of the flow is defined as $Re = UL/\upsilon$ and is equal to 1,600. A periodic cubic domain with a periodicity length of $L_x = L_y = L_z = 2\pi L$ is considered. A uniform grid is adopted with a same resolution in all three directions as $h = 2\pi L/N$, where N is the number of grid cells in one direction. The baseline and refined grid resolutions are 256^3 and 512^3, respectively. The characteristic convective time $(t_c = L/U)$ is defined as the time required for a fluid particle to traverse the characteristic length scale of the flow (L) at the characteristic velocity scale (U). A non-dimensional physical time step of $\Delta t^* = \Delta t/t_c = 0.001$ is adopted for the baseline grid to capture the temporal scales adequately. The physical time step size is halved for the refined grid. The Courant number is set such that $CFL \le 0.1$ for each grid resolution to minimize the temporal error. The simulations are performed for a time period of $t/t_c = 10$.

Different diagnostics are introduced to evaluate the performance of the HDCS6 for the Taylor-Green vortex flow simulation. A common diagnostic is the temporal evolution of the total kinetic energy averaged over the control volume (V):

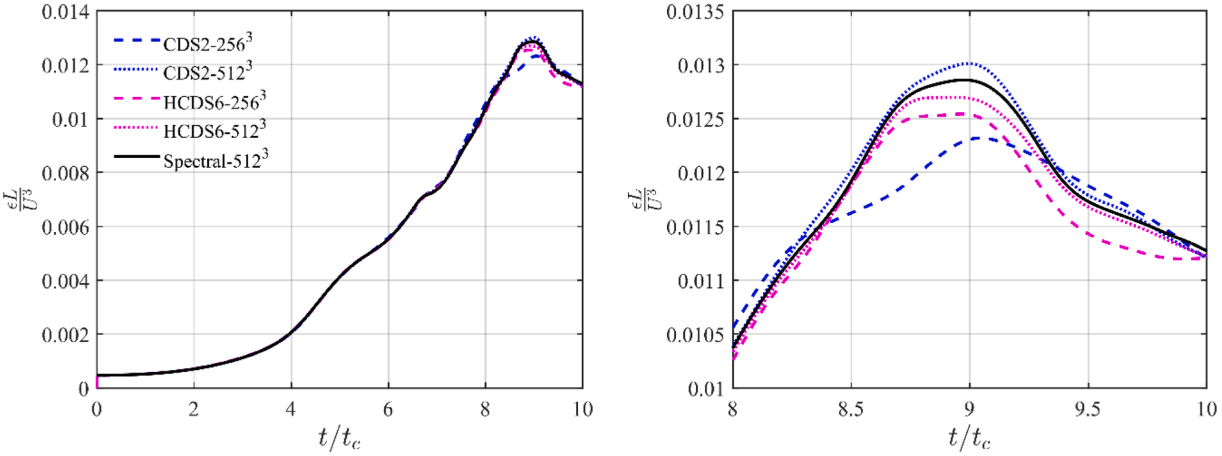

Fig. 6. Temporal evolution of the dissipation rate based on kinetic energy.

$$E_k = \frac{1}{V}\int_V \frac{u_i u_i}{2} dV \tag{18}$$

As the kinetic energy is not expected to vary much between the different scenarios investigated here, the time derivative of the total kinetic energy, defined as kinetic energy dissipation (ϵ), is a more sensitive characteristic than the total kinetic energy:

$$\epsilon = -\frac{dE_k}{dt} \tag{19}$$

A numerical scheme with significant artificial dissipation would fail to reproduce the time evolution of kinetic energy dissipation, making the scheme inappropriate for DNS or explicit LES.

3.2.1. *Verification and consistency*

The evolution of the total volume-averaged kinetic energy was analyzed for two different grid resolutions with 256^3 and 512^3 cells, respectively, and compared with the reference solution from a direct numerical simulation computed using a pseudo-spectral code [34]. Even at the coarsest resolution, the solution from both the CDS2 and the HCDS6 exhibited good agreement with the reference pseudo-spectral solution. However, the temporal evolution of the kinetic energy did not demonstrate sufficient sensitivity to discriminate between the performance of the two central schemes. Therefore, the temporal development of the total kinetic energy dissipation rate is considered as a more discriminating metric.

3.2.2. *Evolution of the dissipation*

Fig. 6 depicts the evolution of the kinetic energy-based dissipation rate using two grid resolutions compared to the reference DNS solution [34]. This is characterized by an initial rapid increase in dissipation rate associated with the formation and stretching of the initial vortices, followed by a gradual decay. As these vortices interact and break down, they transfer energy to smaller scales, thereby increasing the dissipation rate. However, as the flow evolves and the vortices continue to break down, the dissipation rate eventually reaches a steady-state value, which indicates that the energy injection and dissipation are balanced.

To assess the performance of the numerical scheme, a comparison between the CDS2 and HCDS6 on a low-resolution grid (256^3) and a refined grid (512^3) is carried out. At around $t/t_c \approx 4$, the dissipation rate increases rapidly when the transition from simple initial vortices to small-scale anisotropic turbulence occurs. This increase reaches the dissipation peak at around $t/t_c \approx 9$. For the highest under-resolution computation with 256^3 grid cells, the HCDS6 scheme deviates from the pseudo-spectral results around $t/t_c \approx 8.6$ and underpredicts the dissipation peak up to $t/t_c = 10$. The standard CDS2 scheme overestimates the dissipation rate too early at around $t/t_c \approx 7.9$ up to $t/t_c \approx 8.35$ when a significant deviation from the reference data is predicted. From $t/t_c \approx 9$, the dissipation rate gradually decreases until it intersects the pseudo-spectral line at around $t/t_c \approx 9.4$. From now on, the dissipation rate is slightly overestimated up to around $t/t_c = 10$. As the grid is refined, the numerical dissipation rate converges to the reference solution.

3.2.3. *Vortical structures*

Regular counter-rotating vortices stretch and twist as the flow evolves, generating smaller and more complex vortical structures.

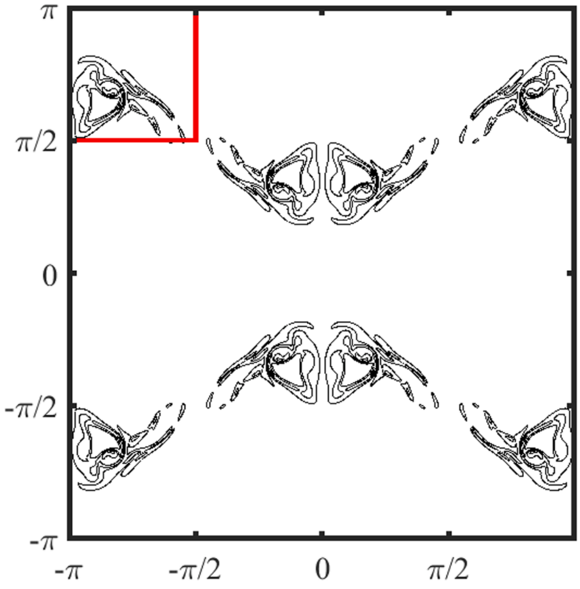

Fig. 7. Instantaneous vorticity norm from the pseudo-spectral scheme on the periodic plane $(\boldsymbol{y} = 0)$ at $\boldsymbol{t}/\boldsymbol{t_c} = 9$.

(a) CDS2, 256^3 (b) CDS2, 512^3

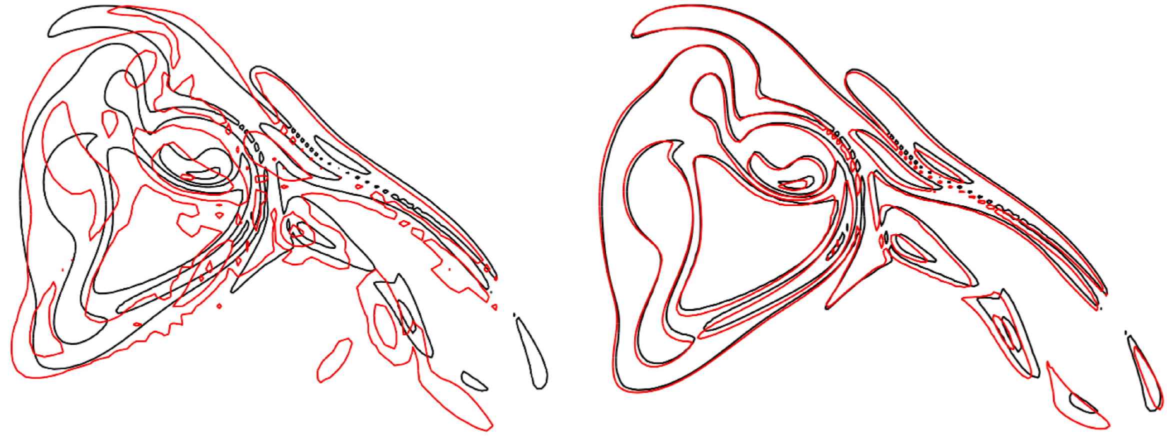

(c) CDS4, 256^3 [34] (d) CDS4, 512^3 [34]

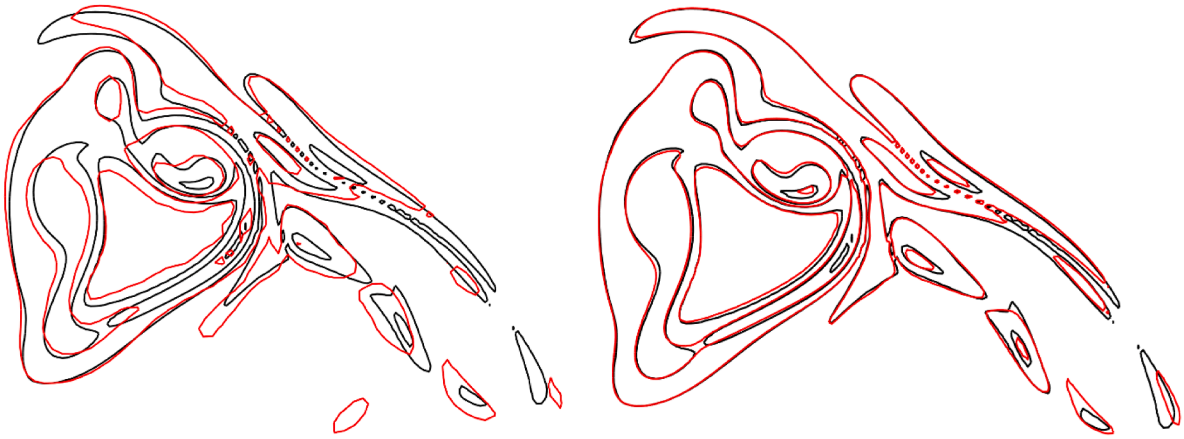

(e) HCDS6, 256^3 (f) HCDS6, 512^3

Fig. 8. Iso-contours of the vorticity norm on the periodic plane ($\boldsymbol{y} = 0$) at $\boldsymbol{t}/\boldsymbol{t_c} = 9$. Spectral solution in black and finite-difference in red. Left: coarse grid (256^3), right: fine grid (512^3).

These structures continue to interact with each other, which creates the most intricate vortices close to the dissipation peak at $t/t_c \approx 9$. A comparison of the instantaneous vorticity field is therefore performed to analyze the accuracy and reliability of the numerical scheme to transport complex vortical structures. It is sufficient to visualize vortical structures on only a limited portion $(1/16)$ of the periodic plane, as the remaining portions will be identical due to different symmetries of the flow [33], as illustrated in Fig. 7.

The vorticity iso-contours for $\omega \in [1, 5, 10, 20, 30]$ on a subset of the periodic plane $(y = 0)$ at $t/t_c = 9$ obtained by CDS2 and HCDS6 schemes are superposed with those from the pseudo-spectral scheme as a reference solution [34] in Fig. 8. For this specific flow diagnostic, the performance of the fourth-order discrete kinetic energy conserving scheme (CDS4) proposed by Vasilyev [11] and provided by M. Duponcheel [34] is also shown. The results are presented for two different grid resolutions of 256^3 and 512^3 in the left and right columns, respectively. On the coarse grid, the position of the large vortical structures is somewhat captured by the CDS2 and CDS4 schemes, while the smaller vortices are diffused and contaminated by numerical noise. The HCDS6 scheme can capture the vortical structures better, although small details of the solution are smeared. The shape of the vortex structure improves and overlaps with the reference spectral solution as the grid is refined using all three schemes. However, the CDS2 scheme still struggles to predict the correct position of vortical structures even on the fine grid.

3.3. Simulation of turbulent channel flows

Numerical simulations of turbulent channel flow are performed to assess the performance of the new HCDS6 scheme. This is an insightful flow benchmark. Firstly, the flow is bounded with a no-slip boundary condition, which generates turbulence. Additionally, previous test cases in this paper were performed on a uniform mesh while, for the channel flow, a grid-stretching is applied in the wall-normal direction. Finally, the under-resolved channel flow is very sensitive to spurious production and dissipation of the discrete kinetic energy. Uncontrolled numerical dissipation strongly impacts the flow statistics, and significant spurious discrete kinetic energy production can lead to numerical instability.

In this benchmark, a fully developed turbulent flow is created between two infinite parallel plates separated by a distance 2δ. A constant adverse pressure gradient is applied to the flow in the streamwise direction to drive the flow through the channel. The no-slip condition is set for the top and bottom walls. Periodic boundary conditions are applied in the streamwise and spanwise directions to approximate infinite homogenous directions. The periodic domain sizes are selected so that the two-point correlations in the streamwise and spanwise directions would be essentially zero at maximum separation (half the domain size). A uniform grid is adopted in the periodic directions, whilst the grid is stretched in the direction normal to the wall in order to properly resolve the boundary layers. This grid-stretching is based on a hyperbolic tangent function:

$$y_j = -\frac{\tanh\left(\gamma\left(1 - \frac{2j}{N_y}\right)\right)}{\tanh\gamma} \quad j = 0, 1, \ldots, N_y \tag{20}$$

where N_y is the number of grid points in the wall-normal direction, and γ is the stretching factor. The mesh is body-fitted, and boundary conditions are introduced using ghost points. A small time step is selected to capture temporal scales precisely and keeps the Courant number below one, guaranteeing numerical stability.

3.3.1. DNS for verification and consistency

In this section, the DNS of a turbulent channel flow at the frictional Reynolds number of $Re_\tau = 180$ is carried out to verify the consistency of the HCDS6 scheme, meaning whether the simulation results converge to the exact solution as the grid resolution is refined. These results are compared to DNS data obtained using a spectral code [35,36].

A same computational domain as that of Moser et al. [36] with $L_x = 4\pi\delta,\ L_y = 2\delta,\ L_z = 4\pi/3\delta$ is used. The grid resolution is $N_x = 256,\ N_y = 256,\ N_z = 256$, where N_x, N_y, and N_z are the number of cells in x, y and z directions, respectively. The stretching factor is equal to 1.6. The corresponding non-dimensional grid spacings in wall units are reported in Table 2.

The computational domain is initialized with a random solenoidal velocity field. The default explicit time integration scheme is not used for this specific test case. A semi-implicit time marching algorithm is rather applied with the implicit Crank Nicholson for the diffusion term and an explicit third-order Runge-Kutta method for the other terms [37]. The bulk time scale $(t^* = L_x/U_b)$ is equivalent to a Flow-Through Time (FTT) of the domain, which corresponds to how long it takes for the fluid to traverse the entire computational domain at a constant mean bulk velocity (U_b). Once the flow has reached a statistical steady state condition, the flow statistics are averaged in the streamwise and spanwise homogeneous directions over a time interval of $50\delta/u_\tau$ approximately equivalent to 37 FTT, which ensures fully converged statistics.

The mean streamwise velocity profile (U^+), the total Reynolds shear stress (T_{xy}), and the square root of the second-order velocity moments normalized by the friction velocity are shown in Fig. 9 as a function of the dimensionless distance to the wall.

The HCDS6 solution is in excellent agreement with the reference DNS results. The mean total Reynolds shear stress compares

Table 2
Channel flow mesh resolution.

Re_τ	Δx^+	Δz^+	Δy^+
180	8.836	2.945	$\in [0.372 - 2.441]$

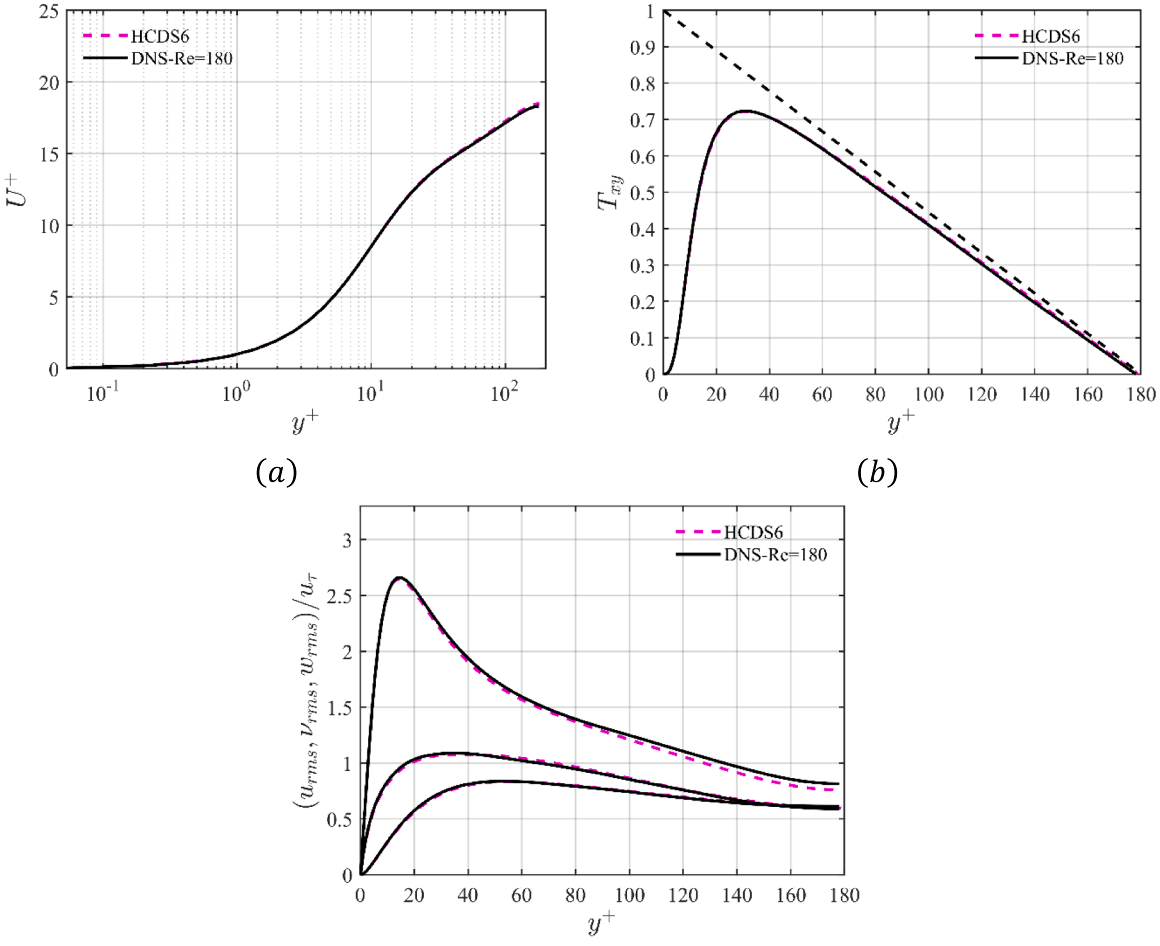

(a) (b)

(c)

Fig. 9. Mean streamwise velocity normalized by the DNS shear velocity (***a***), non-dimensional mean total Reynolds shear stress (***b***), mean normalized square root of the second-order velocity moments (***c***) ($\boldsymbol{u_{rms}}$ (top), $\boldsymbol{v_{rms}}$ (middle), $\boldsymbol{w_{rms}}$ (bottom)) for the DNS of turbulent channel flow at $\boldsymbol{Re_\tau} = 180$.

relatively well with the DNS data shown in the top-right graph in Fig. 9. Investigating turbulence intensities involves analyzing the individual components of the total stress tensor illustrated at the bottom of Fig. 9. The predictions for the spanwise (w_{rms}) and wall-normal (v_{rms}) turbulence-intensity components overlap with the reference DNS of Moser et al. [36]. The streamwise component (u_{rms}) exhibits only a slight deviation for y^+ above 80. All the predictions confirm the consistency of the HCDS6 scheme on non-uniform meshes.

3.3.2. *TNS of the channel flow at* $\mathbf{Re}_\tau = 180,\ 640,\ 950,\ 2000$

In contrast to DNS, which resolves all the turbulent scales, the performance of the HCDS6 in marginally resolved simulations termed Truncated Navier-Stokes Simulations (TNS) is also investigated. In TNS, no turbulence modeling is applied. When a scheme does not conserve the discrete kinetic energy, spurious injection or dissipation of discrete kinetic energy takes place and increases as the simulation gets more under-resolved. TNS thus enables us to investigate whether the lack of discrete kinetic energy conservation affects the HCDS6 performance.

Table 3
Computational domain size and mesh densities for TNS of channel flow at $\boldsymbol{Re_\tau} = 180,\ 640,\ 950,\ 2000$.

Re_τ	L_x	L_y	L_z	N_x	N_y	N_z	Δx^+	Δz^+	Δy^+	γ	FTT
180	$2\pi\delta$	2δ	$\pi\delta$	128	128	128	8.96	4.48	$\in [0.12 - 14.4]$	2.8	42
640	$2\pi\delta$	2δ	$\pi\delta$	128	128	128	31.2	15.6	$\in [0.43 - 29.7]$	2.8	175
950	$2\pi\delta$	2δ	$\pi\delta$	128	128	128	45.7	22.9	$\in [0.63 - 37.1]$	2.8	266
2000	$2\pi\delta$	2δ	$\pi\delta$	128	128	128	99.4	49.7	$\in [1.37 - 58.9]$	2.8	167

The same setup as DNS of turbulent channel flow is carried out at four frictional Reynolds numbers of $Re_\tau = 180,\ 640,\ 950$ and 2000, but on a different computational domain and a coarser mesh. In addition, the grid-stretching is increased compared to the DNS and is made representative of LES applications. The computational domain size, grid resolution, and corresponding non-dimensional grid spacings for each frictional Reynolds number are provided in Table 3.

As the grid is non-uniform with significant grid stretching, the CDS2 does not conserve the discrete kinetic energy. To establish a reference solution for our tests, the skew-symmetric form of the second-order scheme of Vasilyev [11] (given in Eq. (5)) is also simulated since it strictly conserves the discrete kinetic energy on a non-uniform mesh. However, the simulation showed identical results for the divergence and skew-symmetric forms. This aligns with the findings in the channel flow tests conducted by Morinishi et al. [38]. Given that both the divergence and skew-symmetric forms yield the same results, they will not be distinguished and will be simply referred to as CDS2 in this section. It is noteworthy that adjusting the weights of the HCDS6 stencil to accommodate local grid stretching would result in unstable simulations, even at $Re_\tau = 180$.

The mean normalized streamwise velocity profiles for four frictional Reynolds numbers of $Re_\tau = 180,\ 640,\ 950,\ 2000$ along the channel height are shown in Fig. 10. The two discretization schemes agree well with the DNS data at $Re_\tau = 180$. For higher frictional Reynolds numbers, HCDS6 and DNS profiles almost collapse within the viscous sublayer and buffer layer with a slight underprediction in the logarithmic inertial layer. However, the buffer layer, the log layer, and the outer region are strongly affected using the CDS2 scheme, where it starts to deviate from the reference in the buffer layer at $y^+ \approx 10$. At $Re_\tau = 2000$, the grid resolution is insufficient to accurately capture the viscous sublayer, buffer layer and log layer. While HCDS6 tends to overestimate the velocity profile, it manages to capture the accurate shape across the channel height. Conversely, CDS2 struggles to predict the correct velocity profile behavior, and the deviation from DNS data notably increases, particularly in the log layer.

The non-dimensional profiles of mean total Reynolds shear stress at four frictional Reynolds numbers are depicted as a function of the distance from the wall to the center of the channel in Fig. 11. In a fully developed channel flow, the shear stresses and velocity gradients are more significant near the wall, which is indicated by a peak that decreases gradually to the channel centerline as the interaction between the mean velocity profile and the turbulent fluctuations is dampened. For all four frictional Reynolds numbers, CDS2 and HCDS6 can properly reproduce the total Reynolds shear stress of DNS. As the Reynolds number increases in a fully developed

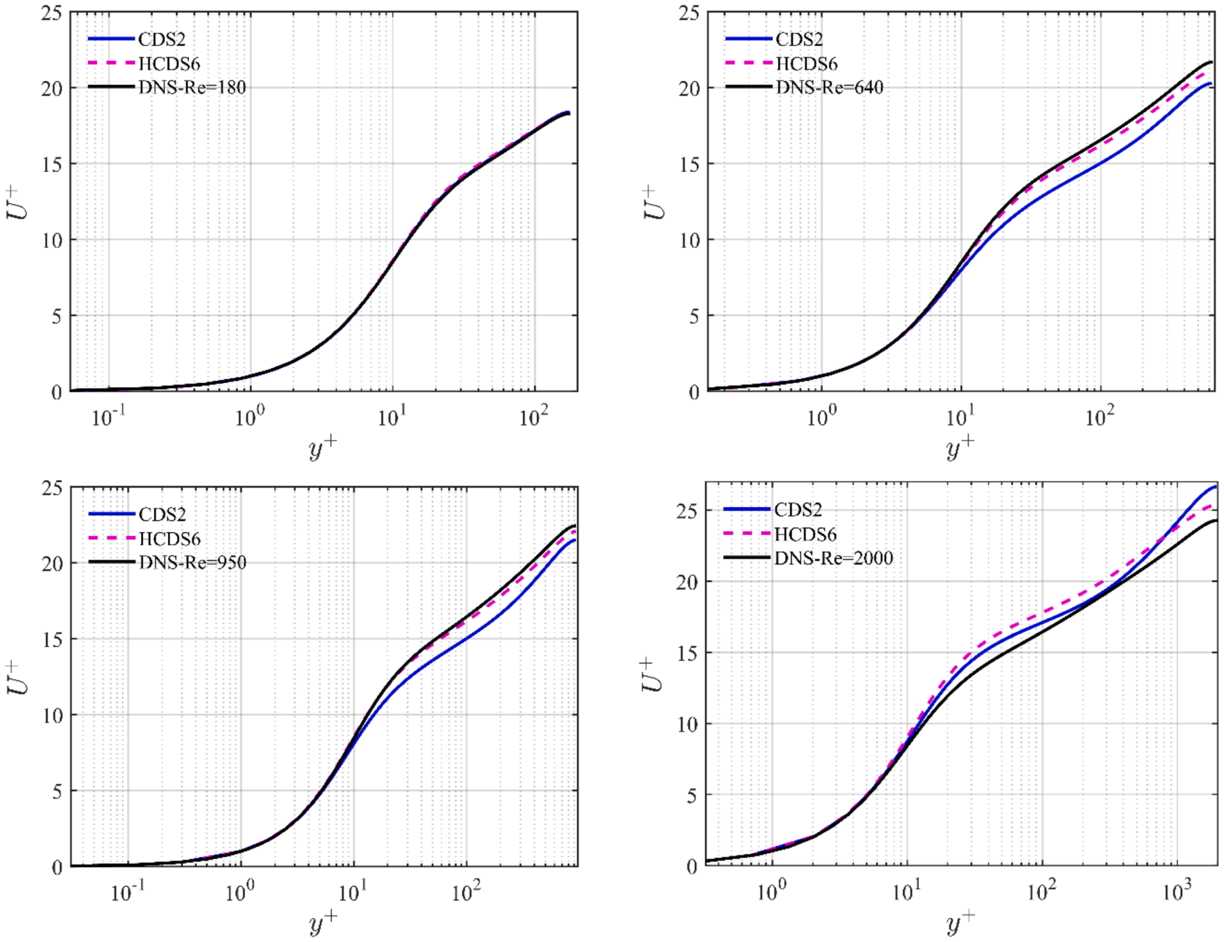

Fig. 10. Mean streamwise velocity normalized by the DNS shear velocity for the TNS of turbulent channel flow at $\boldsymbol{Re_\tau} = 180,\ 640,\ 950,\ 2000$.

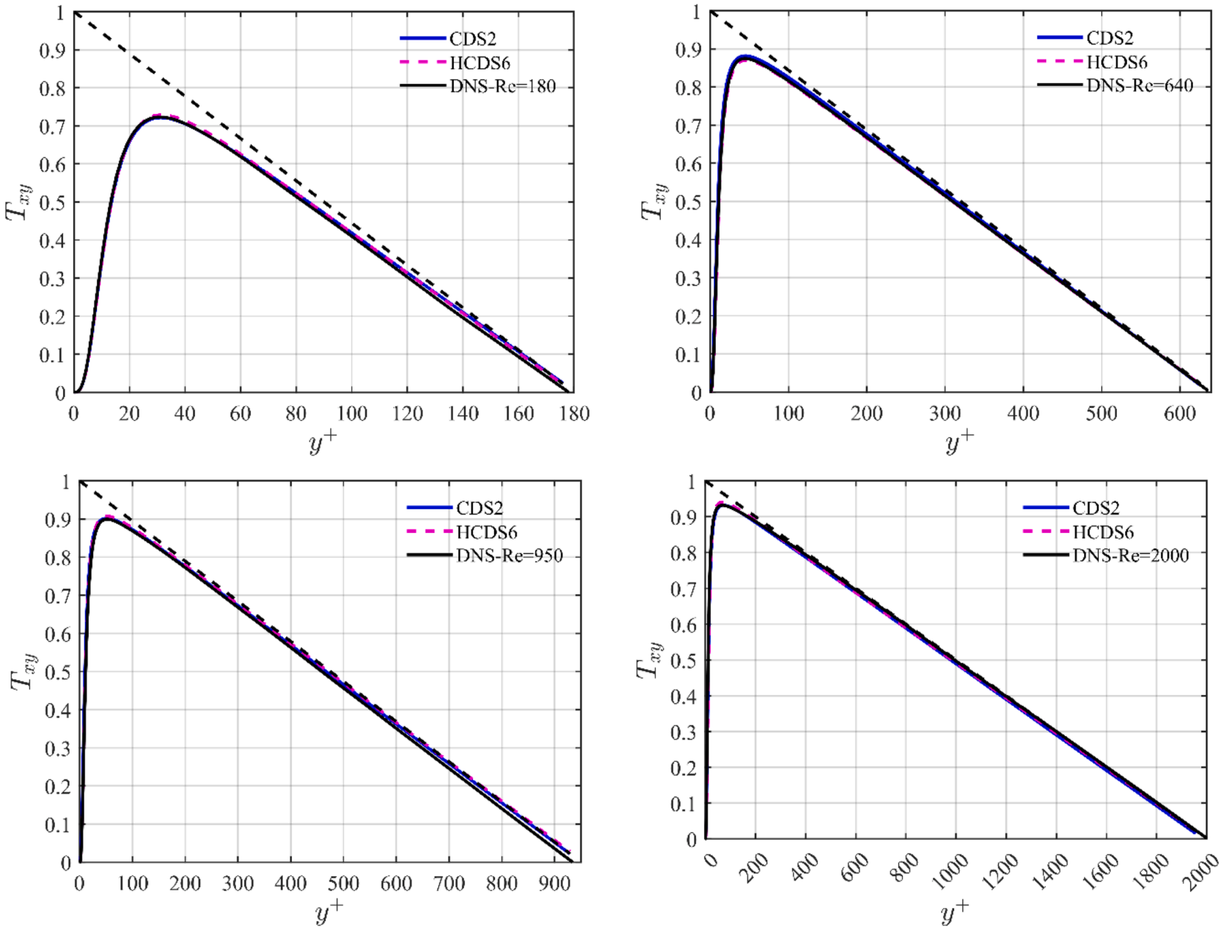

Fig. 11. Non-dimensional mean total Reynolds shear stress for the TNS of turbulent channel flow at $Re_\tau = 180,\ 640,\ 950,\ 2000$.

channel flow, the peak values of the non-dimensional Reynolds stress near the channel walls become more pronounced due to higher turbulence intensity. Moreover, stronger velocity gradients near the walls contribute to a steeper slope of the Reynolds stress profile in this region and promote more efficient mixing and transport of momentum across the flow cross-section. With higher Reynolds numbers, the peak location is shifted toward the wall due to the altered balance between turbulent production and dissipation.

The mean normalized velocity fluctuations of the TNS are compared to DNS data in Fig. 12. For turbulent channel flow at a low Reynolds number of $Re_\tau = 180$, CDS2 performs an excellent job of representing all three components of the total stress tensor in the near wall and core section of the flow. However, the results from HCDS6 predict a slight overprediction, particularly for u_{rms} shear stress distribution when y^+ exceeds 10. By increasing the frictional Reynolds number to $Re_\tau = 640$, all the predictions of HCDS6 for the three velocity fluctuations remain accurate across the channel height, whilst significant deviations from the DNS data are observed for the CDS2 with reduced values of u_{rms} in the buffer and log layers. Both the spanwise and wall-normal components, w_{rms} and v_{rms}, are underpredicted with the CDS2 scheme for the buffer layer and outer region in the core of the flow. The agreement of the turbulent intensity components with DNS at a higher Reynolds number of $Re_\tau = 950$ clearly shows the superiority of the HCDS6 scheme compared to the CDS2. The exception is streamwise stress, u_{rms}, that fails to capture the peak intensity in the vicinity of the wall. The deviation is more pronounced for CDS2, where the elevated prediction of the peak is followed by an underprediction away from the wall. Similarly to $Re_\tau = 640$, wall-normal velocity fluctuation shows an underprediction for wall units of approximately 20 to 210, and it is more pronounced in the outer region for y^+ above 800. Again, HCDS6 successfully reproduces the DNS profile of w_{rms} and v_{rms}. In a highly under-resolved simulation at $Re_\tau = 2000$, streamwise velocity fluctuation swings up and down around the DNS profile using the CDS2 scheme. This indicated that the CDS2 is less reliable as the under-resolution increases. The HCDS6 scheme tends to overpredict the streamwise stress across the channel. Despite this, the overall behavior of HCDS6 remains consistent when compared to the DNS solution, particularly for the other two components of velocity fluctuations.

Two dimensionless gradient-based cell Reynolds numbers evaluated using the norm of vorticity and the strain rate tensor are defined to assess the resolution level of each TNS. The cell Reynolds number based on the vorticity norm ($Re_\Delta - \omega$) and the norm of strain rate tensor ($Re_\Delta - S$) are defined as:

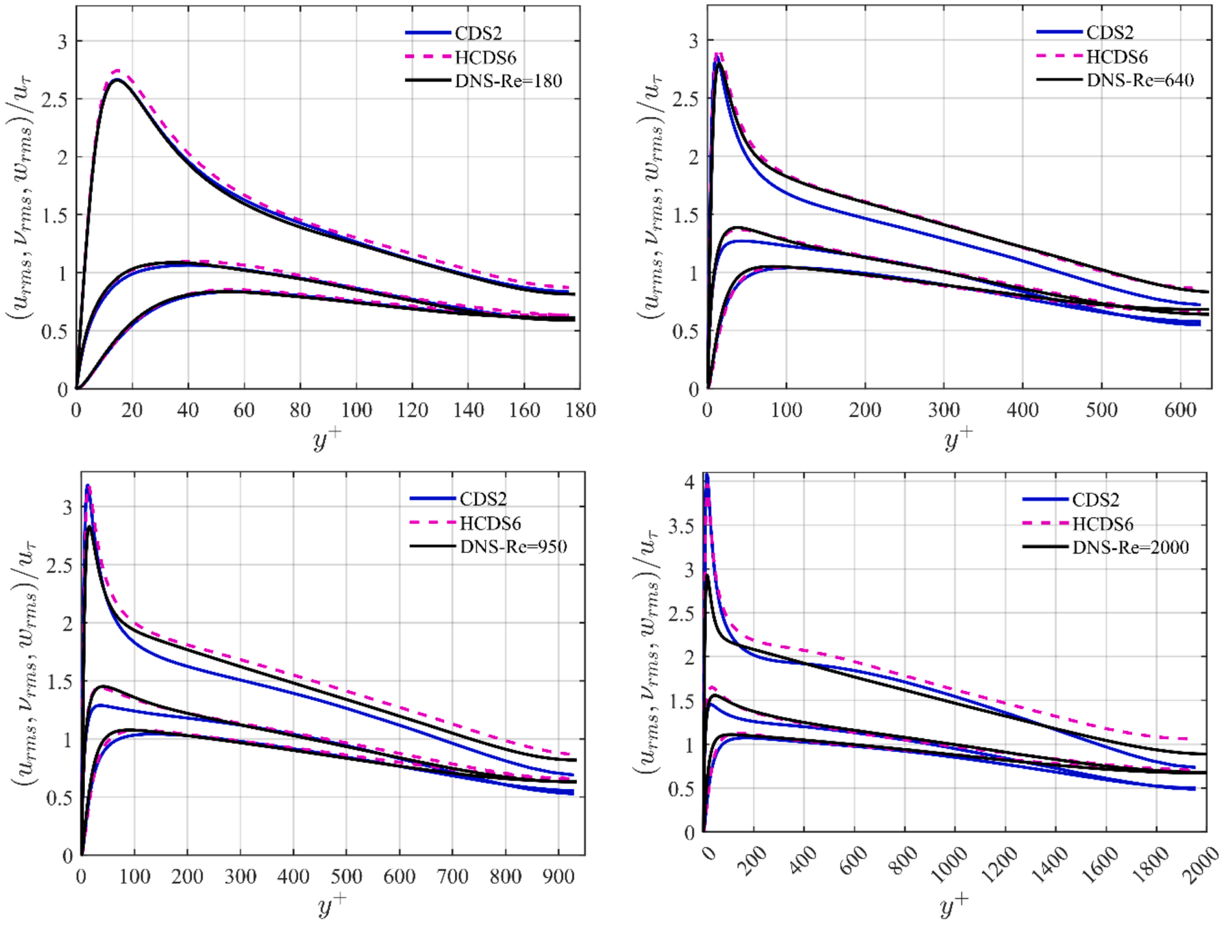

Fig. 12. Velocity fluctuations in streamwise ($\boldsymbol{u_{rms}}$, **top**), wall-normal ($\boldsymbol{v_{rms}}$, **middle**) and spanwise ($\boldsymbol{w_{rms}}$, **bottom**) direction as a function of the distance to the wall ($\boldsymbol{y}^+$) for the TNS of turbulent channel flow at $\boldsymbol{Re_\tau} = 180,\ 640,\ 950,\ 2000$.

$$
\begin{aligned}
Re_\Delta - \omega &= \frac{\langle \omega \rangle \left(\sqrt[3]{\Delta x \Delta y \Delta z}\right)^2}{\upsilon} \sim \left(\frac{\sqrt[3]{\Delta x \Delta y \Delta z} * u_\tau}{\upsilon}\right)^2 \\
Re_\Delta - S &= \frac{\langle S \rangle \left(\sqrt[3]{\Delta x \Delta y \Delta z}\right)^2}{\upsilon} \sim \left(\frac{\sqrt[3]{\Delta x \Delta y \Delta z} * u_\tau}{\upsilon}\right)^2
\end{aligned}
\tag{21}
$$

where $\langle \omega \rangle$ represents the vorticity magnitude and $\langle S \rangle$ denotes the strain rate magnitude averaged along homogeneous directions. $\sqrt[3]{\Delta x \Delta y \Delta z}$ is the characteristic cell size based on the cell volume. Δx, Δy, and Δz are the cell dimensions in x, y, and z directions, respectively.

The profiles of the mean cell Reynolds numbers across the channel height using the HCDS6 scheme are shown in Fig. 13. As expected, the cell Reynolds numbers increase with the Re_τ. They reach a maximum value in the laminar sublayer and then decrease to a relatively flat profile towards the center of the channel. The following argument demonstrates that the TNS is well under-resolved for $Re_\tau = 2000$:

- At the wall, the vorticity is equal to the gradient of the streamwise velocity component with respect to y, leading to $Re_\Delta - \omega = (\Delta y^+)^2$. In a wall-resolved DNS or LES, the typical recommended near-wall resolution is $\Delta y^+ \sim 1$. This value is lower or close to 1 in the four TNS, as shown in Table 3. However, the cell Reynolds number exhibits a peak value in the vicinity of the wall. This peak increases by a factor of 50 from the TNS at $Re_\tau = 180$ to $Re_\tau = 2000$.
- In the center of the channel, the flow is comparable to homogeneous isotropic turbulence (HIT). Then, the value taken by the cell Reynolds number of a LES for a HIT can be considered as a reference point for our TNS. In a LES of decaying homogeneous isotropic turbulence (DHIT) at high Reynolds numbers using the Smagorinsky subgrid-scale model, the theory predicts that the model constant (C_s) should be equal to 0.027. This is equivalent to a $Re_\Delta - S$ of about 37 when evaluated on the subgrid-scale eddy viscosity. In a study by Thiry et al. [39], a LES of the DHIT is performed using the dynamic Smagorinsky model. The Taylor

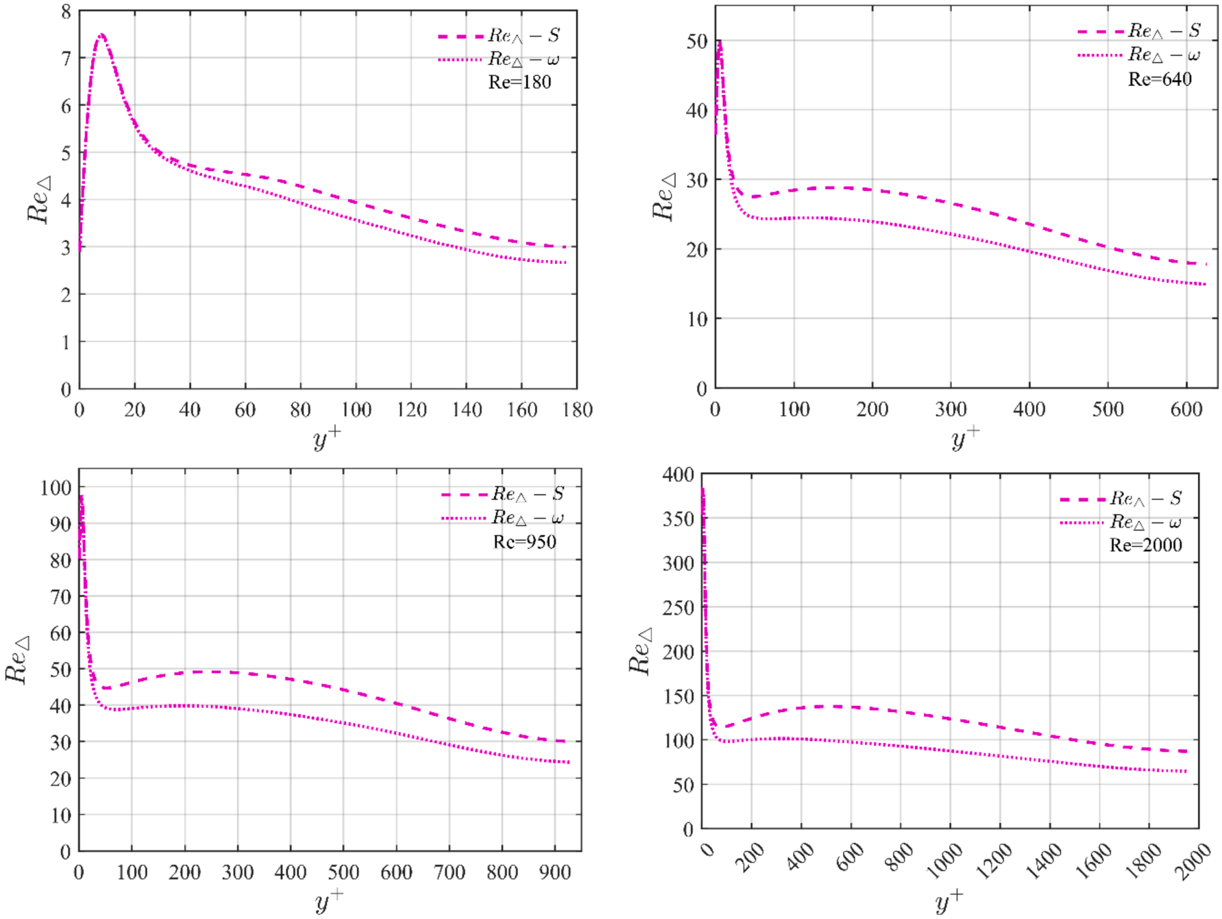

Fig. 13. Mean cell Reynolds number based on vorticity ($\boldsymbol{Re_\Delta} - \boldsymbol{\omega}$) and strain term ($\boldsymbol{Re_\Delta} - \boldsymbol{S}$) as a function of the distance to the wall ($\boldsymbol{y}^+$) for the TNS of turbulent channel flow at $\boldsymbol{Re_\tau} = 180,\ 640,\ 950,\ 2000$.

micro-scale Reynolds number was taken very large (i.e., υ_{SGS}/υ converges to infinity), and the DHIT was computed on a 512^3 mesh using a pseudo-spectral method. The C_s evaluated by the dynamic procedure was then equal to 0.0115, well lower than the theoretical constant. This value corresponds to a $Re_\Delta - S$ of about 87 based on the subgrid-scale eddy viscosity. For the TNS at $Re_\tau = 2000$, the $Re_\Delta - S$ has a value of about 100 near the center of the channel when HCDS6 is adopted. This indicates that the level of under-resolution reached by the TNS at $Re_\tau = 2000$ is representative of a LES at very high Reynolds number in the center of the channel flow.

In conclusion, when a scheme does not conserve the discrete kinetic energy, the resulting spurious production or dissipation of discrete kinetic energy increases with the level of under-resolution. Even though the TNS at $Re_\tau = 2000$ is under-resolved near the wall and has a resolution comparable to LES at high Reynolds number in the center of the channel, the HCDS6 scheme is not affected by the non-conservation of the discrete kinetic energy. As previously shown, the flow statistics predicted by the HCDS6 are similar to the standard second-order scheme of Vasilyev in the skew-symmetric form that strictly conserves the discrete kinetic energy. It is also worth mentioning that a significant spurious injection of discrete kinetic energy would eventually make the simulation unstable. This is not the case for our simulations when the HCDS6 scheme is adopted.

4. Conclusions

A new second-order finite-difference scheme (HCDS6) was introduced to discretize the convective terms of the incompressible Navier-Stokes equations on an orthogonal non-uniform staggered grid. This scheme is expressed in divergence form and conserves the discrete mass and momentum with limited production or dissipation of discrete kinetic energy. Compared to the standard second-order scheme, the proposed scheme is more accurate. Compared to existing fourth-order kinetic energy-conserving schemes, the new scheme has a numerical stencil that is more compact, which makes its implementation and the treatment of boundary conditions easier.

The scheme performance was evaluated on viscous and inviscid flow simulations conducted on both uniform and non-uniform grids. In a grid-convergence analysis for the advection of an isentropic vortex, the RMS of the vortex velocity using the HCDS6 scheme was reduced by two orders of magnitude compared to the standard second-order central scheme. For the Taylor-Green vortex flow, iso-contours of the vorticity norm in the midplane close to the dissipation peak were compared with a DNS reference solution. Here, complex vortical structures were better captured by the HCDS6 than by the standard second-order scheme. The under-resolved turbulent channel flow benchmark was a challenging case for investigating the stability and accuracy of the scheme on a non-uniform grid. Simulations showed that the HCDS6 remained stable even if the simulations were getting highly under-resolved (by increasing the frictional Reynolds number to 2000). The flow statistics were comparable to the standard second-order scheme, which strictly conserves discrete kinetic energy. It proved that, even though the HCDS6 does not strictly conserve the discrete kinetic energy, it does not affect the numerical stability and flow statistics.

The new scheme is thus an alternative to the existing central scheme for incompressible flow on staggered meshes. It can facilitate the use of staggered grids in combination with complex geometries modeled using Immersed Boundary Methods (IBM).

CRediT authorship contribution statement

Elyas Larkermani: Writing – review & editing, Writing – original draft, Visualization, Validation, Software, Resources, Methodology, Investigation, Formal analysis, Conceptualization. **Hans Bihs:** Supervision, Software, Methodology. **Grégoire Winckelmans:** Validation, Supervision, Methodology, Investigation, Conceptualization. **Matthieu Duponcheel:** Validation, Methodology, Investigation, Conceptualization. **Tobias Martin:** Writing – review & editing, Software, Investigation. **Bernhard Müller:** Writing – review & editing, Validation, Supervision, Methodology, Investigation. **Laurent Georges:** Writing – review & editing, Validation, Supervision, Software, Resources, Project administration, Methodology, Investigation, Formal analysis, Conceptualization.

Declaration of competing interest

The authors declare that they have no known competing financial interests or personal relationships that could have appeared to influence the work reported in this paper.

Data availability

Data will be made available on request.

Appendix

For an initial condition $u(x,0) = e^{ikx}$, the exact solution of the linear advection equation (Eq. (9)) on the spatial domain $x \in [0, 2\pi]$ with periodic boundary conditions:

$$u(x,t) = e^{ik(x-at)} \tag{22}$$

is admitted. Here, k is the wavenumber.

The numerical solution can be expressed in terms of its Fourier series:

$$u_j(t) = \sum_k u_k(t) e^{ikx_j} \tag{23}$$

where u_k is the amplitude of the k^{th} Fourier mode.

The Fourier transform of the semi-discretized Eq. (11) is obtained by substituting $u_j(t)$ from Eq. (23):

$$\frac{\partial u_k(t)}{\partial t} e^{ikx_j} = -\frac{a u_k(t)}{2h} \left(\frac{1}{30} e^{3ikh} - \frac{3}{10} e^{2ikh} + \frac{3}{2} e^{ikh} - \frac{3}{2} e^{-ikh} + \frac{3}{10} e^{-2ikh} - \frac{1}{30} e^{-3ikh} \right) e^{ikx_j} \tag{24}$$

and is simplified using Euler's formula $\left(e^{\pm ikh} = \cos kh \pm i \sin kh\right)$:

$$\frac{\partial u_k(t)}{\partial t} = -\frac{ai}{h} \left(\frac{1}{30} \sin(3kh) - \frac{3}{10} \sin(2kh) + \frac{3}{2} \sin(kh) \right) u_k(t) \tag{25}$$

The solution of Eq. (25) in Fourier space can be written as:

$$u_k(t) = e^{-\frac{ai}{h}\left(\frac{1}{30}\sin 3kh - \frac{3}{10}\sin 2kh + \frac{3}{2}\sin kh\right)t} \tag{26}$$

Substituting this expression into Eq. (23), the numerical solution can be obtained in physical space:

$$u_j(t) = \sum_k e^{i\left(kx_j - \frac{at}{h}\left(\frac{1}{30}\sin(3kh) - \frac{3}{10}\sin(2kh) + \frac{3}{2}\sin(kh)\right)\right)} \tag{27}$$

Comparing the exact and numerical solutions of the 1D linear advection equation (Eqs. (22) and (27)), the non-dimensional modified wavenumber $\widetilde{k}_{mod} = k_{mod}h$ reads as a function of the non-dimensional wavenumber $\xi = kh$:

$$\widetilde{k}_{mod} = \frac{1}{30}\sin(3\xi) - \frac{3}{10}\sin(2\xi) + \frac{3}{2}\sin(\xi) \tag{28}$$

The dispersion relation ($\omega = k_{mod}a$), the phase velocity (ω/k) and the group velocity ($d\omega/dk$) become:

$$\begin{aligned} \omega &= \frac{a}{h}\left(\frac{1}{30}\sin(3\xi) - \frac{3}{10}\sin(2\xi) + \frac{3}{2}\sin(\xi)\right) \\ \frac{\omega}{k} &= \frac{a}{\xi}\left(\frac{1}{30}\sin(3\xi) - \frac{3}{10}\sin(2\xi) + \frac{3}{2}\sin(\xi)\right) \\ \frac{d\omega}{dk} &= a\left(\frac{1}{10}\cos(3\xi) - \frac{3}{5}\cos(2\xi) + \frac{3}{2}\cos(\xi)\right) \end{aligned} \tag{29}$$

To ensure a comprehensive analysis, the phase speed anisotropy is evaluated following the procedure outlined by Lele [24]. Fig. 14 illustrates that the HCDS6 outperforms the CDS2 for all angles of the propagation direction (θ) and wavenumbers.

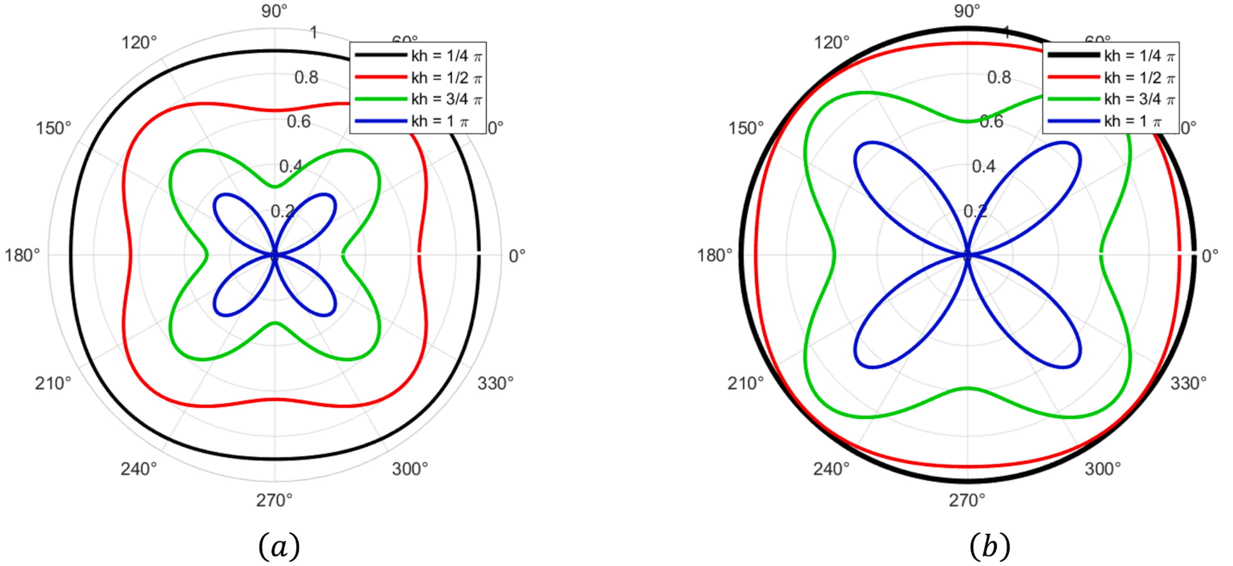

Fig. 14. Polar plot of phase speed anisotropy for the CDS2 (a) and HCDS6 (b) for different wavenumbers ($\pi/4$, $\pi/2$, $3\pi/4$) and (π).

References

[1] R. Mittal, G. Iaccarino, Immersed boundary methods, Annu. Rev. Fluid Mech. 37 (2005) 239–261.
[2] Yalla, G.R., *Numerical discretization effects in large eddy simulation of turbulence*. 2022.
[3] A. Kravchenko, P. Moin, On the effect of numerical errors in large eddy simulations of turbulent flows, J. Comput. Phys. 131 (2) (1997) 310–322.
[4] S. Ghosal, An analysis of numerical errors in large-eddy simulations of turbulence, J. Comput. Phys. 125 (1) (1996) 187–206.
[5] J.W. Glendening, T. Haack, Influence of advection differencing error upon large-eddy simulation accuracy, Boundary. Layer. Meteorol. 98 (2001) 127–153.
[6] F.K. Chow, P. Moin, A further study of numerical errors in large-eddy simulations, J. Comput. Phys. 184 (2) (2003) 366–380.
[7] J. Gullbrand, F.K. Chow, The effect of numerical errors and turbulence models in large-eddy simulations of channel flow, with and without explicit filtering, J. Fluid. Mech. 495 (2003) 323–341.
[8] C. Canuto, et al., Spectral methods: fundamentals in single domains, Springer Science & Business Media, 2007.
[9] S. Nagarajan, S.K. Lele, J.H. Ferziger, A robust high-order compact method for large eddy simulation, J. Comput. Phys. 191 (2) (2003) 392–419.
[10] S. Laizet, E. Lamballais, High-order compact schemes for incompressible flows: A simple and efficient method with quasi-spectral accuracy, J. Comput. Phys. 228 (16) (2009) 5989–6015.
[11] O.V. Vasilyev, High Order Finite Difference Schemes on Non-uniform Meshes with Good Conservation Properties, J. Comput. Phys. 157 (2) (2000) 746–761.
[12] R. Verstappen, A. Veldman, Symmetry-preserving discretization of turbulent flow, J. Comput. Phys. 187 (1) (2003) 343–368.
[13] S. Armfield, Finite difference solutions of the Navier-Stokes equations on staggered and non-staggered grids, Comput. Fluids. 20 (1) (1991) 1–17.
[14] E.M.J. Komen, et al., Analysis of the numerical dissipation rate of different Runge–Kutta and velocity interpolation methods in an unstructured collocated finite volume method in OpenFOAM®, Comput. Phys. Commun. 253 (2020) 107145.
[15] F.H. Harlow, J.E. Welch, Numerical calculation of time-dependent viscous incompressible flow of fluid with free surface, Phys. fluids 8 (12) (1965) 2182–2189.
[16] F. Ham, F. Lien, A. Strong, A fully conservative second-order finite difference scheme for incompressible flow on nonuniform grids, J. Comput. Phys. 177 (1) (2002) 117–133.
[17] P. Moin, R. Verzicco, On the suitability of second-order accurate discretizations for turbulent flow simulations, Eur. J. Mech.-B/Fluids 55 (2016) 242–245.
[18] P. Orlandi, A numerical method for direct simulation of turbulence in complex geometries, Ann. Res. Briefs 1990 (1989) 215–229.

[19] M. Duponcheel, P. Orlandi, G. Winckelmans, Time-reversibility of the Euler equations as a benchmark for energy conserving schemes, J. Comput. Phys. 227 (19) (2008) 8736–8752.
[20] E. Kálnay de Rivas, On the use of nonuniform grids in finite-difference equations, J. Comput. Phys. 10 (2) (1972) 202–210.
[21] T.A. Manteuffel, A.B. White, The numerical solution of second-order boundary value problems on nonuniform meshes, Math. Comput. 47 (1986) 511–535.
[22] Z. Tian, X. Liang, P. Yu, A higher order compact finite difference algorithm for solving the incompressible Navier–Stokes equations, Int. J. Numer. Methods Eng. 88 (6) (2011) 511–532.
[23] Y. Morinishi, et al., Fully conservative higher order finite difference schemes for incompressible flow, J. Comput. Phys. 143 (1) (1998) 90–124.
[24] S.K. Lele, Compact finite difference schemes with spectral-like resolution, J. Comput. Phys. 103 (1) (1992) 16–42.
[25] P.A. Berthelsen, O.M. Faltinsen, A local directional ghost cell approach for incompressible viscous flow problems with irregular boundaries, J. Comput. Phys. 227 (9) (2008) 4354–4397.
[26] Y.-H. Tseng, J.H. Ferziger, A ghost-cell immersed boundary method for flow in complex geometry, J. Comput. Phys. 192 (2) (2003) 593–623.
[27] H. Bihs, et al., A new level set numerical wave tank with improved density interpolation for complex wave hydrodynamics, Comput. Fluids. 140 (2016) 191–208.
[28] A.J. Chorin, Numerical solution of the Navier-Stokes equations, Math. Comput. 22 (104) (1968) 745–762.
[29] H.A. Van der Vorst, Bi-CGSTAB: A fast and smoothly converging variant of Bi-CG for the solution of nonsymmetric linear systems, SIAM J. Sci. Stat. Comput. 13 (2) (1992) 631–644.
[30] R.D. Falgout, J.E. Jones, U.M. Yang, Conceptual interfaces in hypre, Fut. Gener. Comput. Syst. 22 (1-2) (2006) 239–251.
[31] C.-W. Shu, S. Osher, Efficient implementation of essentially non-oscillatory shock-capturing schemes, J. Comput. Phys. 77 (2) (1988) 439–471.
[32] E. Weinan, J.-G. Liu, Projection method I: convergence and numerical boundary layers, SIAM. J. Numer. Anal. (1995) 1017–1057.
[33] L. Bricteux, S. Zeoli, N. Bourgeois, Validation and scalability of an open source parallel flow solver, Concur. Comput.: Pract. Exp. 29 (21) (2017) e4330.
[34] C. Carton de Wiart, et al., Assessment of a discontinuous Galerkin method for the simulation of vortical flows at high Reynolds number, Int. J. Numer. Methods Fluids. 74 (7) (2014) 469–493.
[35] J. Kim, P. Moin, R. Moser, Turbulence statistics in fully developed channel flow at low Reynolds number, J. Fluid. Mech. 177 (1987) 133–166.
[36] R.D. Moser, J. Kim, N.N. Mansour, Direct numerical simulation of turbulent channel flow up to Re τ= 590, Phys. Fluids 11 (4) (1999) 943–945.
[37] H. Le, P. Moin, An improvement of fractional step methods for the incompressible Navier-Stokes equations, J. Comput. Phys. 92 (2) (1991) 369–379.
[38] Y. Morinishi, et al., Fully Conservative Higher Order Finite Difference Schemes for Incompressible Flow, J. Comput. Phys. 143 (1998) 90–124.
[39] O. Thiry, G. Winckelmans, M. Duponcheel, *The Dynamic Smagorinsky Model in Pseudo-Spectral LES of Decaying Homogeneous Isotropic Turbulence at Very High*, in *Direct and Large-Eddy Simulation XI*, Springer, 2019, pp. 123–128.